SISSA ISAS

SCUOLA INTERNAZIONALE SUPERIORE DI STUDI AVANZATI
INTERNATIONAL SCHOOL FOR ADVANCED STUDIES

Simulation of Iron at Earth's Core Conditions

Thesis submitted for the degree of

"Doctor Philosophiæ"

CANDIDATE

Alessandro Laio

SUPERVISORS

Guido Chiarotti

Sandro Scandolo

Erio Tosatti

October 1999

Contents

Acknowledgments

Dopo quattro anni trascorsi qui a Trieste, le persone a cui sono grato per quanto mi hanno dato dal punto di vista scientifico sono veramente tante.

Prima di tutto, voglio ringraziare Stephane Bernard. Questo lavoro e' anche "suo", se non altro per aver condiviso con me molti momenti difficili...

Un grazie veramente doveroso a Carlo Cavazzoni: senza il suo aiuto e il suo codice questo lavoro sarebbe stato semplicemente impossibile.

Sandro Scandolo e Guido Chiarotti, oltre che essere stati i migliori collaboratori che uno possa desiderare, sono stati per me degli ottimi amici.

Un grazie a Erio Tosatti per il suo contagioso entusiasmo per la fisica, e per gli innumerevoli (e preziosissimi) suggerimenti.

Voglio infine ringraziare Giuseppe Santoro e Vincent Torre che, pur non essendo direttamente coinvolti in questo lavoro, sono comunque stati estremamente importanti per la mia formazione in questi anni.

Introduction

The deep interior of the Earth is inaccessible, and almost everything we know about its structure, history and evolution is not entirely based on direct observation but rather on models that, although constructed by keeping into account well assessed physical laws (e.g. the laws of thermodynamics and fluidodynamics), require a constant interplay with the science of materials at high pressure in order to asses their validity and predictivity. Just to give an example, an Earth's core thermal model requires, in order to be predictive, detailed knowledge of the thermal conductivity of Earth's core material.

The most important source of direct information concerning the interior of our planet is provided by seismology. Since it was born as a science, at the beginning of this century, seismology produced a revolution in our knowledge of the interior of the Earth. By using seismic waves velocity profiles, Williamson and Adams, in 1921[1] were able to show that the simple increase of rocks' density due to pressure is not sufficient to explain an average density of the Earth of 5.5 gr/cm^3, starting from a density at the surface of 3-3.5 gr/cm^3. Thus, they concluded that "the dense interior cannot consist of ordinary rocks compressed to a small volume; we must therefore fall back on the only reasonable alternative, namely, the presence of an heavier material, presumably some metal, which, to judge from its abundance in the Earths crust, in meteorites and the Sun, is probably iron".

Nowadays, the foreseeing claim by Williamson and Adams, has been confirmed by a lot of observations. It was by comparing density data as deduced from seismological measurements and from shock wave experiments that Birch in 1961[2] was able to show that the Earth's core is mainly composed of iron diluted with light elements. His principal argument was that silicates, although very abundant, could never achieve the density of the core, as given by seismology, unless under pressures much larger than the Earth's interior pressure. Iron, Birch observed, is instead the only element of relatively great abundance whose density at Earth's core pressures is comparable with the Earth's core density. Moreover, since the density of pure iron at core pressures is slightly smaller than the core density, Birch concluded that a few percent of lighter elements was necessary to bring the density exactly to the core value.

Birch's original reasonings were based on informations provided *both* by seismology and by materials science: major advances in our understanding of Earth's deep interior are always linked to major advances in experimental or theoretical techniques in seismology or high-pressure physics. The claim by Williamson & Adams [1] concerning the composition of the Earth's core could be confirmed by Birch only thanks to the development of shock-wave techniques to measure the density of materials at very high pressure.

An other important example of the interplay between seismology and materials science is the construction of the temperature profile as a function of depth inside the Earth. In fact, while density and pressure can be quite reliably deduced from seismological measurements, there is no way to estimate the temperature inside the Earth by seismology alone. The only way to constrain the temperature in the deep interior of the Earth is to measure the pressure-temperature curves

for phase transitions responsible for the major seismic discontinuities: it is well known from seismology that the innermost 1200 kilometers of the core are solid (the so-called inner core), while its remaining portion (the outer core) is liquid. The boundary between these two regions is called the inner core boundary (ICB), and the pressure at this boundary is approximately 330 GPa[3]. Since the Earth's core is mainly composed of iron, at the ICB solid and liquid iron coexist; thus, the melting temperature of iron at ICB pressure (330 GPa) is an estimate of the temperature of the Earth at ICB (for a more accurate value, the effect of lighter elements in the core should also be considered [4]).

Other quantities of major geophysical relevance, whose estimate can be provided only by high-pressure physics, are the elastic properties of iron (both liquid and solid) at Earth's core conditions, the thermal conductivity coefficient and the viscosity of liquid iron at outer core conditions.

All the above quantities, as well as the effect that light alloying elements may have on them, are of primary importance for any modeling of the Earth's interior.

The task to estimate these quantities has proved a very difficult one for both experimentalists and theorists. Up to date, despite major efforts, only few of these quantities are known to a level of accuracy sufficient to solve most of the outstanding geophysical problems

The current knowledge of the high pressure properties of iron will be reviewed in Chapter 1.

For the time being, let we just mention that estimates of the melting temperature of iron at ICB pressure range between 4000 and 8000 K and, also due to this large temperature uncertainty, the density of liquid and solid iron at core conditions is known only roughly. The phase and the elastic behavior of iron at inner

core pressures are known only at room temperature and are still the subject of speculations at temperatures close to melting (exotic proposals such as a glassy structure or a partial melt [5] have also been suggested for the inner core). The situation is even less clear for what concerns the effect that lighter elements have on the properties of pure iron at core pressures. In most cases, the high pressure binary diagram of iron with a light element are extrapolated from the zero pressure behavior, or ideal mixing conditions are assumed.

First-principle molecular dynamics has proved to be an invaluable tool to explore the high temperature properties of many systems, because of its superiority in terms of accuracy and predictivity[6]. Unfortunately, in our case (iron at high pressure and temperature) a correct description of the electronic structure is computationally very demanding, as we shall see in Chapter 2. Moreover, even for simpler systems, such as silicon, a standard first-principle molecular dynamics approach can seldom be used to fix the value of the melting temperature, because of unavoidable size effects and because of the poor statistical sampling due to the short simulation times that can be afforded with first-principle simulations.

On the other hand, molecular dynamic simulations with classical empirical potentials would overcome sampling and finite size problems [7]. Of course, as was correctly stated in a recent article about first principle calculations on iron, simulations based on empirical potentials suffer "from the lack of reliability that can be placed on using potentials beyond the range of empirical fitting" and, therefore, "the confidence with which one can predict properties outside the experimental range" is small[8].

In this work we propose a novel method for handling classical potentials for iron with a procedure that, in our opinion, successfully overcomes the first-

principle-versus-empirical dilemma. In particular, in our procedure (introduced and discussed in detail in Chapter 3), the potential is fitted ”in flight” to forces and stress calculated on first-principle trajectories *at the desired pressure-temperature (P-T) thermodynamic point only* (and not on a large set of properties of bulk, defects, surfaces, clusters, liquids in a wide range of pressures and temperatures, as in standard fitting procedures). This ”optimal” potential is then used to extract dynamical and thermodynamical informations on the system at given P-T conditions without limitations of size or simulation time.

Since only the dynamics at a single P-T point is described, the accuracy of the fit can be very good, and the thermodynamic observables extracted from trajectories generated with the optimal potential can be pushed to an accuracy comparable to that obtained with an ab-initio approach (see Chapter 3 for a detailed analysis of this point). This is obtained at the cost of a very poor transferability of the optimal potential to P-T conditions different from the ones where it has been constructed. No attempt is made to construct a potential that describes iron at all conditions, and when considering a new P-T point, a new potential must be generated. Potentials constructed with our procedure are then explicitly dependent on the P-T thermodynamic conditions. When a phase transition is encontered at the given P-T point (e.g. melting), the request will be that the two potentials constructed for trajectories on both sides (e.g. the solid and the liquid) yield the same transition temperature.

In Chapter 4, the method outlined above is applied to the calculation of some of the properties of iron at conditions of relevance for the Earth’s core. Our results are compared with experiments, where available. The comparison shows that our method reproduces with very good accuracy the experimental equation

of state and the elastic properties at room temperature and along the shock-wave compression line (the so called Hugoniot). This comparison is particularly relevant for assessing the validity of the method, since these quantities are known experimentally with very small uncertainties. Our method proves able to reproduce densities with an accuracy of ~ 1 % and elastic properties with an accuracy of ~ 3 % both at low temperature and at high temperature (along the Hugoniot). These accuracies are comparable with those expected from the best fully ab-initio simulations.

We will consider in detail the melting line of iron between 100 and 330 GPa, showing that our values are compatible, within at most 300 K, with the best measurements at low pressures (up to ~ 100 GPa) and that the melting temperature at ICB pressure is 5400 ($\pm$ 150) K.

We will also show that elastic properties of solid iron in a hexagonal close-packed (hcp) structure at inner core conditions are perfectly compatible with seismic observations. Moreover, we will provide an accurate estimate of the liquid and solid iron density at ICB conditions. Results concerning other observables related to the melting, such as the heat of cristallization and the density jump, will also be presented and their geophysical implications discussed.

Chapter 1

Physics of Iron and Physics of the Earth's Core

The interplay between material science (in particular the physics of iron) and physics of Earth's deep interior has become more and more important, and the two subjects are so deeply entangled that extensive calculations or measurements of iron properties at high pressure conditions are considered essential to provide informations to construct reliable models of the Earth's core. This Chapter is dedicated to an overview on the current knowledge of high-pressure physics of iron and its relation to geophysics.

In Section 1.1, some of the properties of iron at high-pressure high-temperature conditions that are of particular interest for geophysics and that will be studied in some details in this work are listed. We will consider the high pressure melting line, the density of solid and liquid iron at inner core boundary conditions, the heat of crystallization and the elastic property of solid iron at high pressure. What it is currently known about these properties from the experimental and theoretical point of view is then reviewed in the following two sections.

1.1 Constraint to models of the Earth from physics of iron.

1.1.1 Melting temperature

The Earth's temperature distribution is intimately connected to problems of structure, composition, dynamic state and evolution of the planet. High temperature sustains the Earth's convection, and is responsible for the strong geological activity observed at the surface[9]. Despite this importance, the temperature profile inside the Earth is known only very roughly: at variance with density, temperature is in fact quite poorly constrained by seismological observations[10]. The only way to safely estimate the temperature inside the Earth is to predict its value at phase transitions responsible for seismic discontinuities[9]. For example, the inner core boundary (ICB) separates the inner core, mainly composed of solid iron, from the outer liquid core. Since it is known from standard seismological models[3] that the inner core boundary is at a pressure of 330 GPa, the melting temperature of iron at this pressure crucially constrains the temperature at the ICB, and provides a valuable pinning point for every thermal model of the Earth. We shall see in Section 1.2.3 that this quantity, despite a great experimental and theoretical effort, is presently known only roughly.

The situation is further complicated by the presence, at least in the outer core, of some percent of impurities (as we will discuss in next subsection). Due to the presence of these impurities, the temperature at the ICB will be different from the melting temperature of pure iron at 330 GPa. This difference can be easily estimated only if ideal solubility conditions are assumed, as shown in Section 4.3. A more accurate estimate would require a very precise knowledge of the

composition of the outer core[11] and of the iron-rich part of multicomponent diagrams of iron with the impurities.

1.1.2 Density of the IC and OC

By x-ray diffraction experiments in the diamond anvil cell, Mao *et al* estimated, in 1991, the room-temperature density of iron at 330 GPa[12] obtaining a value of 13.87 gr/cm^3. This density is ~ 10 % higher than the density of the outer core at the ICB (12.17 gr/cm^3) extracted from seismological data [3]. A further indication that the density at the ICB is sensitively smaller than the density of pure iron is given by the shock-wave measurements of density by Brown and McQueen[13] (see Section 1.2.2). In their experiment, the density of shocked liquid iron at 333 GPa is shown to be 12.92 gr/cm^3, i.e. ~ 6 % larger than the seismological value.

The exact value of the density difference between pure iron and the outer core material constrains the quantity of light elements that alloy with iron in the outer core[14], with the implications we mentioned on the temperature at ICB. A second (and possibly even more relevant) consequence of the presence of light elements in the outer core is that a concentration gradient due to crystallization of the liquid iron alloy in the more pure inner core might sustain mass convection. This mechanism could contribute sensitively to the geodynamo energy budget, as suggested for the first time by Loper in 1978[15]. Values for this density difference currently accepted in the literature range between 7 and 10 %[9, 11, 16].

Also the inner core is probably alloyed by a small amount of impurities, as suggested by Jephcoat[17]. The exact percentage of these impurities can be estimated given the density of pure solid iron at ICB conditions.

An accurate theoretical determination of solid and liquid iron density at 330

GPa is at present missing, and could shed some light on the above issues.

1.1.3 Heat of crystallization.

Since the Earth is cooling, the liquid iron alloy of the outer core is slowly crystallizing in the more pure iron of the inner core. The rate of this freezing process can be estimated by thermal models of the Earth and determines the age of the inner core (according to a recent estimate, this age is ~ 1.7 Gyears or less[18]; an earlier estimate by Stacey was of 4 Gyears [9]). The crystallization process releases heat that might contribute sensitively to the Earth energy budget, as suggested by some authors[4, 9]. The relevance of this energy release with respect to other possible sources of energy (e.g. the mass convection) depends on the rate of growth of the inner core and on the value of the heat of crystallization ΔH_m. The value of ΔH_m is closely related to the melting line slope (by the Clausius-Clapeyron relation), and it has been estimated only by simplified models of melting or by thermodynamic consideration[4, 19].

1.1.4 Elastic properties

The inner core is known to be elastically anisotropic [20, 21]. In particular, longitudinal waves (P-waves) propagate in the inner core with greater velocity parallel to the Earth's rotation axis than in the equatorial plane. This difference can be explained with a ~ 3 % elastic anisotropy of the inner core.

Among the possible explanations of this anisotropy [22], one of the most reasonable hypothesis is that the anisotropy could derive from some degree of preferential orientation in the high-pressure phase of iron present in the inner core. It was recently shown, both theoretically and experimentally, that hcp crystals

of iron at high pressure and room temperature condition are indeed anisotropic with respect to P-wave propagation[5, 23]. In particular, Stixtrude and Cohen estimated, with a first-principle calculation[23], an anisotropy of $\sim$10 % up to ICB pressures, in very good agreement with the recently revised experimental data by Mao *et al*, available up to 210 GPa[5] (see section 1.2.1 and 1.3).

A high-temperature estimate of P-wave anisotropy for hcp iron is at the moment missing. If iron remains in the room temperature hcp phase also at inner core conditions, and if we assume the room temperature value for the hcp anisotropy, the degree of alignment of the iron crystalline domains in the inner core required to provide the observed 3 % anisotropy would be as large as ~ 40 %. This may have important consequences on accretion models for the inner core[22].

Another elastic quantity of great relevance is the value of the shear modulus of iron at inner core conditions. In fact, it is well known that shear waves propagate in the inner core at a very low speed, compared to compression waves[3], leading to a Poisson ratio of ~ 0.45, very close to the shear-less value of 0.5. In particular, the value of the shear modulus B_S corresponding to the observed velocity of shear waves v_s is $\sim$160 GPa, approximately three times smaller than the value measured at room temperature[3]. This behavior is in some way anomalous, with respect to other transition metals (in most of the metals, at least at ambient pressure, B_s is approximately two times smaller at the melting temperature with respect to the room temperature value[24]). This has led many authors to suggest that low-shear phases (other than hcp) might be present in the inner core[5, 25], or, alternatively, that the inner core could be partially molten[5], with very important consequences for accretion models of the core. A direct (experimental or theoretical) determination of B_s for hcp iron at ICB conditions would be very useful to validate these

suggestions.

1.2 Physics of iron at core conditions: experiments.

In this section the most important experimental findings on the high pressure physics of iron are overviewed. The geophysical interest of the argument has stimulated, in the last 20 years, an enormous amount of experimental work. Although our understanding of the properties of high-pressure Fe has greatly improved , we are still far from an exhaustive comprehension, at least at the level of accuracy required to solve geophysical issues.

The phase diagram of iron is fully understood only at pressures lower than 20 GPa (see Figure 1.1). Four phases are well known in this pressure range: α-Fe (bcc), the magnetic ambient condition phase of iron; γ-Fe (fcc) at high temperature and low pressure; δ-Fe (bcc) close to the melting point and at low pressure; ε-Fe (hcp) at low temperature and pressures above 13 GPa. At higher pressure, several different melting curves and phase diagrams have been proposed by different authors, leading to estimates of the melting temperature at ICB ranging from 4000 to 8000 K. The state-of-the-art concerning this very important issue will be reviewed in Section 1.2.3. Among the few well-constrained experimental quantities, we can list the room temperature equation of state (reviewed in Section 1.2.1) and the value of density and sound velocities along the shock-wave compression line (Section 1.2.2).

1.2.1 Room temperature EOS and Elastic constants

Mao *et al* in 1990 measured the volume of hcp iron up to $\sim$ 300 GPa with x-ray diffraction[12]. Their results confirmed and extended the measurements by Jephcoat *et al* [26] up to 70 GPa. Mao et al. also found virtually no difference between the P-V results of a nickel $Fe_{0.8}$-$Ni_{0.2}$ alloy and those on pure iron up to 300 GPa. The P-V experimental points of Mao *et al* are reported in Fig. 1 of Chapter 2. More recently, Mao *et al* measured the room temperature elastic constants of hcp iron up to 210 GPa using radial X-ray diffraction and ultrasonic techniques[5]. The observed compressional wave anisotropy is $\sim$ 8 %, in agreement with theoretical calculations by Cohen *et al* [23]. Their elastic constants at 211 GPa are reported in Table I of Section 4.1. [1]

1.2.2 Shock-wave compression line

The sound velocity and density measurements along the shock-wave compression line (the so-called Hugoniot EOS) for iron up to $\sim$ 400 GPa by Brown and McQueen in 1985[13] is one of the cornerstones in the high P-T physics of iron.

In a standard shock-wave experiment, the shock-wave velocity (U_s) and the velocity imparted to the particles of the sample by the shock wave (U_p) are directly measured. Pressure P, internal energy E and density ρ during the shock are then deduced from U_s and U_p through Hugoniot-Rankine relations[10] (see Section 4.5). Since Hugoniot-Rankine are deduced with the only assumption of conservation of mass, momentum and energy in the shocked sample, the value of

[1] Very recently, Singh and Montagner[27] pointed out some inconsistencies in this set of data, such as a very low (0.04) Poisson's ratio along the symmetry axes. Therefore, they suggest to interpret these data with some caution.

P, ρ and E estimated with a shock-wave experiment is considered very reliable and accurate.

Brown and McQueen extended this method to allow also the measurement of the longitudinal sound velocity v_P in the shocked sample. Since a phase transition usually causes only a minor kink in the P-versus-ρ curve, but can produce a marked discontinuity in the v_p-versus-P curve, this method provided a powerful tool to explore the high-pressure phase diagram of iron.

Brown and McQueen observed that v_P along the Hugoniot grows with pressure up to ~ 200 GPa, where a first kink is observed (see Figure 4.4); a second kink is observed at ~ 240 GPa, and above ~ 280 GPa v_P reduces to $\sqrt{B_v/\rho}$, where B_v is the adiabatic bulk modulus and ρ is the density, indicating that the sample is completely liquid. The first kink is interpreted by Brown and McQueen as a solid-solid phase transition (from ε-Fe to an unknown phase), the second as the onset of melting.

By assuming reasonable values for the Gruneisen parameter γ and for C_v, Brown and McQueen also provide an estimate of the temperature along the Hugoniot. Their estimate is based on simple thermodynamics and does not keep into account phase transitions, so it has to be considered as reliable only up to the first transitions point at 200 GPa. Moreover, the accuracy of this estimate of temperature is limited by the uncertainties on C_v and γ.

The observation of a double kink along the Hugoniot of iron (see Figure 4.4) has been considered for a long time a strong evidence for the existence of an additional high-pressure high-temperature phase (other than ε-Fe), and this has stimulated a large amount of theoretical and experimental research. Nevertheless, as we will see in the following, the existence of this phase is still very controversial.

The second kink observed by Brown and McQueen may rather be a by-product of the phase coexistence between the solid and the liquid, as suggested by MD simulations performed on Argon by Belonoshko[28]. Moreover, very recent sound velocities measurements along the iron Hugoniot by Nguyen *et al*[29] seem to cast some doubt on the very existence of a double kink: sound velocities between 220 GPa and 280 GPa decrease, in Nguyen *et al* data, almost monotonically, with no apparent discontinuity in between.

1.2.3 Melting line and high-pressure high-temperature phases of iron

The phase diagram of iron at pressures higher than 20 GPa is still the subject of strong controversy. Some of the melting curves presented by different authors are shown in Figure 1.

Below ~ 200 GPa, the melting temperature has been measured in static experiments using diamond-anvil-cells (DAC). Above this pressure, the melting temperature can be determined only by dynamic shock-wave experiments in which the high pressure and density conditions are reached instantaneously by shooting an impactor on the sample.

The first measurement of the iron melting line performed with a DAC is due to Williams *et al* in 1987[30]. Melting is detected in their experiment by a visual observation of the samples after the laser is switched off (keeping the sample at high pressure), assuming that, if a change of texture is observed, the sample has crossed the melting line. They measure the melting temperature up to $\sim$ 100 GPa, estimating a melting temperature at this pressure of more than 4000 K. Their melting line connects nicely with higher pressure measurements performed

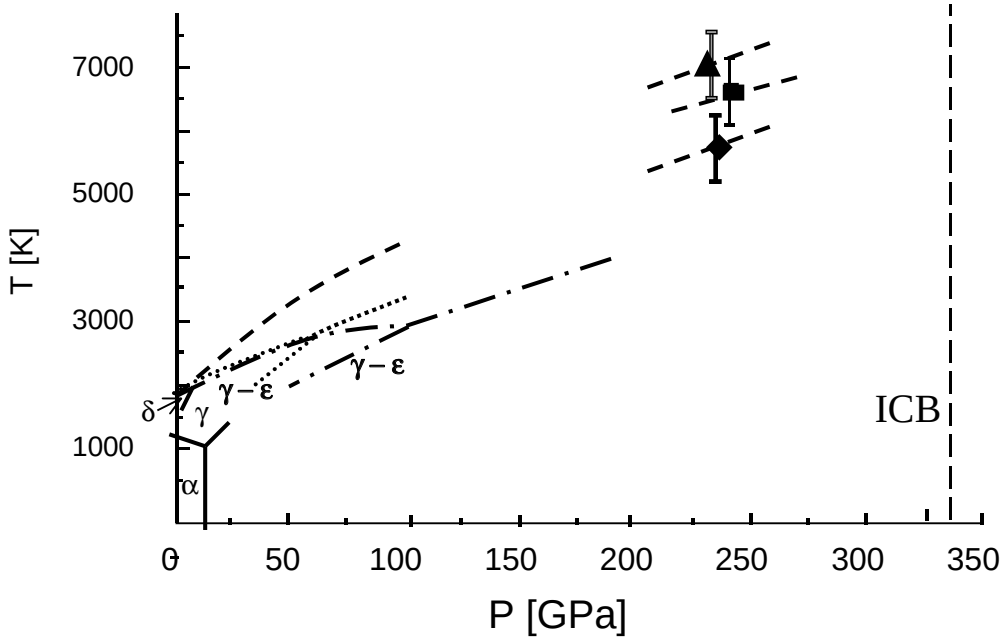

Figure 1.1: Experimental phase diagram of iron. Full lines: phases boundaries of iron below 20 GPa.

Lines: diamond-anvil cell data on the melting line of iron and the $\gamma - \varepsilon$ phase-boundary. Dashed line: data by Williams *et al* [30]. Dot-dashed line: data by Boehler *et al* [31] and by Saxena *et al* [32] (up to $\sim$ 120 GPa). Dotted line: data by Shen *et al* [33].

Dashed lines with error bars and symbols: shock wave data on the melting of iron along the Hugoniot. Triangle: data by Bass *et al* [34, 35]. Square: data by Yoo *et al* [36]. Diamond: data by Brown and McQueen [13] and by Gallagher and Ahrens [37].

by shock-wave techniques (see Figure 1.1). Unfortunately their results have not been confirmed by more recent DAC measurements.

The most extensive measurements of the melting line of iron in a DAC are due to the Mainz group. Their experiments at high pressure are done by plating the iron sample on a ruby disk immersed in a pressure medium made of ruby powder. The sample is heated by a laser. Temperature is measured fitting the radiation from iron through the ruby disk to a Planck's radiation function. Melting is detected visually as the onset of convective motion. Boehler *et al* in 1990 [38] reported the melting temperature of iron up to 120 GPa and found the triple point connecting the ε (hcp), γ (fcc), and liquid phases at about 100 GPa and 2800 K. The existence of this triple point is deduced, in Boehler's experiments, by the change in curvature in the solid-liquid boundary. In 1993, Boehler extended his measurements on T_m up to 190 GPa[31], finding at this pressure a T_m of about 3800 K. In 1994 he confirmed the existence of the triple point at 100 GPa by experimental data showing all the three branches[39].

Saxena *et al*, in 1994[32], using a diamond-anvil cell apparatus similar to that of the Mainz group, obtained experimental results on the melting line of iron up to 60 GPa, confirming the curve of Boehler *et al*. In Saxena *et al*'s experiments, melting is detected by the abrupt change at T_m in the slope of temperature versus laser power (due to the heat of melting).

Boehler's curve was further confirmed in 1994 in a DAC experiment performed by Yoo *et al*[40]. The disappearance of the crystalline X-ray diffraction lines was used in these experiments as a criterion to detect the melting transition. These data have to be taken with some caution since, as claimed by Shen *et al* [33], the absence of crystallographic structure does not necessarily imply melting.

The experiment by Yoo *et al* was repeated and extended by Shen *et al* in 1998 [33]. According to their measurements, the ε-γ-liquid triple point is at 60($\pm$5) GPa and 2800($\pm$200)K, i.e. at a lower pressure than Boehler suggested. Their melting line is defined, at every pressure, by the highest temperature where crystalline phases is observed, and lies approximately 300 K above Boehler's melting line (with approximately the same slope).

All the DAC data concerning the melting line obtained by Boehler *et al*, Saxena *et al*, Yoo *et al* and Shen *et al* are compatible with each other (within an error bar of 300 K), with the exception of the early DAC experiment by Williams *et al* that gives a completely different melting line slope and a melting temperature almost 1000 K higher at 100 GPa.

The melting temperature of iron at pressure higher than 200 GPa has been estimated only by shock-wave experiments. The first estimate of T_m along the Hugoniot was given, as we already mentioned in Section 1.2.2, by Brown and McQueen[13], who reported a solid-liquid phase transition at 243 GPa and 5400 K. In this work, however, T is not directly measured, but only estimated.

The melting temperature has been directly measured in a shock wave experiment by the CalTech group (Bass *et al* and Ahrens *et al*)[34, 35] and by the Livermore gruoup in 1993[36]. Their results concerning the temperature along the Hugoniot are in quite good agreement except for the highest pressure datum (at 300 GPa). At 300 GPa, Bass *et al* report a temperature of 9000 K, approximately 1500 K higher than the Yoo *et al* result (see Figure 4.5). Both the CalTech group and the Livermore group use shock wave radiance to estimate the temperature. In particular, in both experiments the intensity of radiation from shocked iron at a given pressure is measured versus frequency, and the temperature is deduced

using the Stefan's law. Melting is detected as a lateral displacement in temperature along the Hugoniot. Bass *et al* estimate in this way a melting temperature of ~ 7000 K at ~ 240 GPa[34]. Yoo *et al* of 6500 K, also at 240 GPa[36]. These values are more than 1000 K higher than Brown and McQueen's estimate and 2000 K higher than the extrapolation of the DAC melting lines. If both the DAC and the shock wave data were correct, the melting line slope between 200 and 240 GPa should be unphysically high[31].

The simplest possible explanation of the discrepancy is that the shock wave temperatures are overestimated. This opinion, shared by a part of the shock-wave community[35, 37], is based on the fact that the radiation emitted from shocked iron, before being detected by the frequency analyzer, passes through a dielectric block (Al_2O_3), and the thermal diffusivity of this material can change the spectrum of emitted light. This makes a direct measurement of T along the Hugoniot quite complicated and possibly affected by large systematic errors. In 1994, Gallagher and Ahrens presented new data , based on better estimates of thermal diffusivity in Al_2O_3, that lowered the calculated values of the melting temperature of iron by approximately 1000 K from those proposed by Bass et al., bringing T_m at 240 GPa down to ~ 5500 K[37], i.e. very close to the Brown and McQueen estimate.

If this value of T_m is correct, the slope in the melting line required to connect this point with the upper DAC measurement of Boehler[31] would still be very large but not unphysical. Nonetheless, the presence of a triple point in the vicinity of 200 GPa should be assumed, as only a triple point can explain a sharp increase in the melting line slope[41]. This might be also consistent with the long-sought solid-solid phase transition observed by Brown and McQueen at 200 GPa along the Hugoniot. Since in this pressure and temperature range no x-ray

measurement have been performed so far, the nature of this new phase has only been suggested by theoretical calculations. Many authors (in particular, Ross *et al* [42] and Matsui *et al*[25]) suggested for this phase a bcc structure. However, in recent first-principle calculations, the bcc phase was shown to be mechanically unstable at zero temperature (see Section 3) and to be disfavored with respect to hcp by $\sim$ 540 meV/atom [43]. This very large energy difference is believed to rule out bcc as a possible high temperature phase of iron in the pressure range considered[41, 44].

The high-pressure high-temperature phase diagram of iron is further complicated by the possible presence of another phase between ε-Fe and γ-Fe at pressures above $\sim$ 30 GPa. The presence of this new phase was first suggested by Saxena *et al*, in 1993[45]. They observe, always by the laser-power versus T method, a new phase boundary from $\sim$ 1000 K and 30 GPa to $\sim$ 2000 K and 130 GPa. They suggest that this new phase might form a large part of the Earth's core. This phase (of unknown crystallographic structure) was named β-Fe. In 1995[46], they proposed for this phase a dhcp structure: they observed that laser heated iron, quenched from high temperature up to $\sim$ 1500 K at 30 to 40 GPa, transforms to a dhcp structure. Yoo *et al*[47] confirmed the observation in 1996, at pressure below 40 GPa. However, more recent measurements do not confirm these observations: in the same pressure field, Andrault *et al* observed, in 1997, an orthorhombic structure[48]. Moreover, Shen *et al* [33], in their x-ray study on melting, do not observe new phases in the pressure and temperature range of interest, and they conclude that the appearance of new structures is probably an effect of temperature gradients in Saxena *et al* and Andrault *et al* experiments.

From this short overview, it should emerge that experimental evidences con-

cerning the high pressure phase diagram of iron above 20 GPa are still quite ambiguous, and at least three different scenarios are possible:

- The shock wave temperatures (including Ahrens data) are overestimated by 1000 K or more. The DAC melting line continues monotonically without any need for a triple point. Iron in the inner core has an hcp (or β) structure.

- The DAC melting temperature is underestimated (by ~ 1000 K or more at 200 GPa). The melting line is shifted upward to the shock wave values and no new phase is necessary above 200 GPa. Even in this case, iron in the inner core has an hcp (or β) structure.

- DAC measurements and shock wave estimates of T_m by Gallagher and Ahrens[37] and Brown and McQueen[13] are correct. A triple point with a new phase of unknown crystallographic structure exists at $\sim$ 200 GPa. Iron in the inner core has the structure of this new phase. This scenario would reconcile the greatest number of experimental observations.

The phase diagrams resulting in these three cases are sketched in Figure 1.2. The hypothetical phase boundary between ε and β phase is also reported in these diagrams for completeness. We will see in Chapter 4 that our calculations suggest that the correct scenario is the first one (no definitive indication concerning the existence of the β phase is provided by our theory).

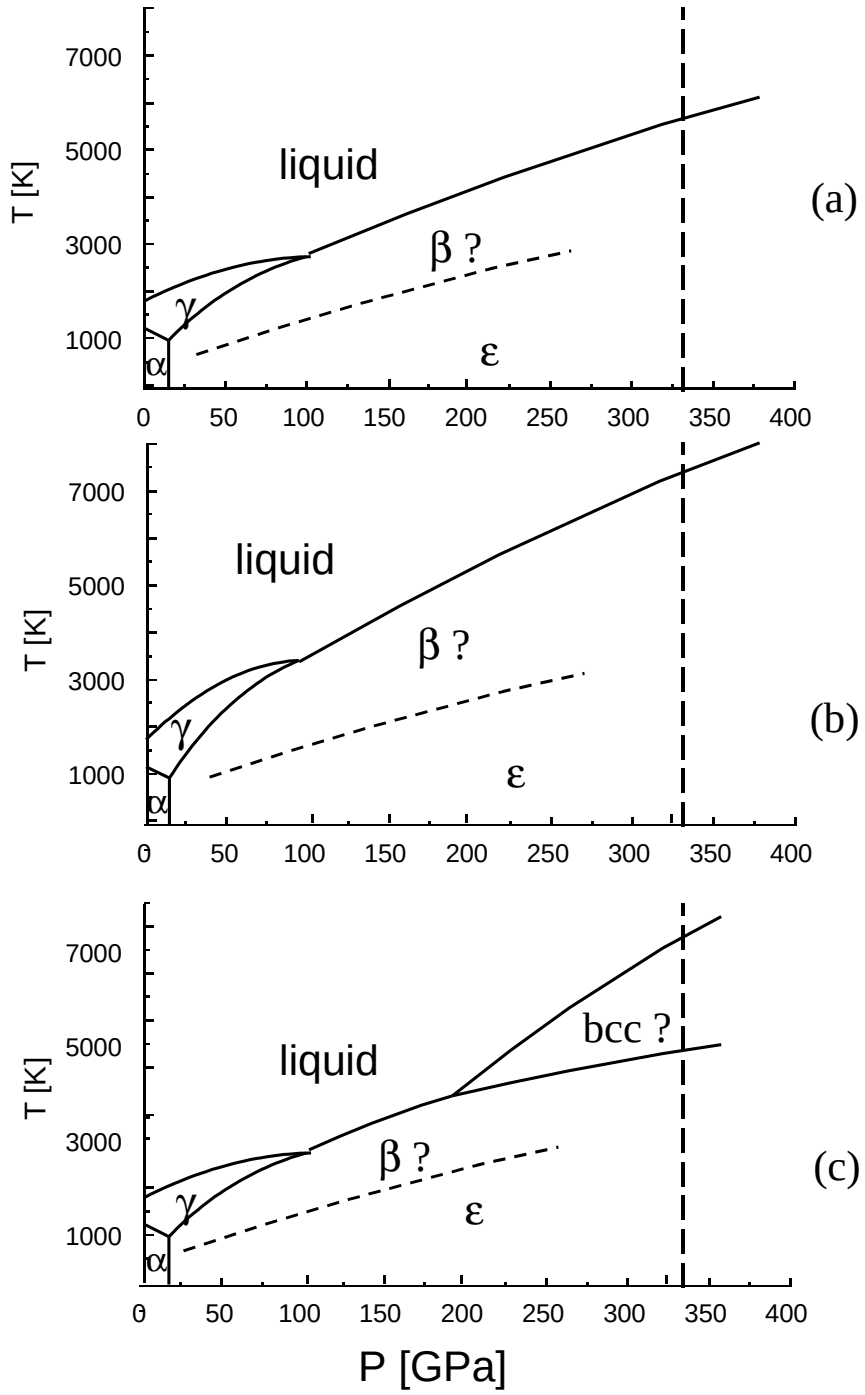

Figure 1.2: Three possible speculative scenarios for the high-pressure phase-diagram of iron. The inner core boundary pressure is indicated as a dashed line. The hypothetic $\varepsilon - \beta$ phase boundary is also reported. Results in this thesis will support scenario (a), however with no definitive indication concerning the existence of the β phase.

1.3 Physics of iron at core conditions: first principle simulations

The evergrowing interest in the physics of iron at Earth's core conditions has stimulated a great number of first-principle-based theoretical studies aimed to determine some of the basic properties of iron at high pressure and high temperature. At least some of these properties, such as the zero-temperature equation of state, elastic constants and phase stability, are nowadays well understood at a theoretical level. Density functional theory is able to reproduce all the measurable experimental quantities with a very satisfactory level of accuracy, thus encouraging the application of the same methodologies to finite temperature properties. Unfortunately, this has proved quite an ambitious goal, due to intrinsic difficulties in a fully ab-initio modelization of iron. The only high temperature properties studied by ab-initio methods so far are the transport and the structural properties in the liquid phase[49]. In the liquid, ab-initio methods were used to *predict* some quantities of geophysical relevance, otherwise unaccessible to experimental measurements (in particular the viscosity). In this Section, we will recall some of the results obtained up to now and the technical details of the ab-initio implementation used.

Some of the earliest ab-initio calculations on solid iron were performed by Jansen *et al*[50, 51] in 1994. They concluded that the use of the local density approximation or local spin-density approximation are not sufficient to describe the structural and magnetic property of iron with good accuracy.

A significant improvement was reported by Stixrude *et al* in 1994, who showed that by the inclusion of the generalized gradient approximation[52, 53] (GGA)

excellent agreement with the experimental room temperature equation of state of bcc and hcp iron can be obtained[54]. Also the bcc-hcp transition pressure and the bcc magnetic moment are correctly reproduced within their approach.

In 1995, Stixrude and Cohen[23] presented results on high-pressure elastic constants of iron, using a tight-binding approach (the parameters of tight binding Hamiltonian are fitted to first-principles band structures and total energies of fcc, hcp and bcc). With this method, they show that, at the density of the inner core, hcp phase of iron is substantially ($\sim$ 8 %) elastically anisotropic.

A complete theoretical investigation of the zero-temperature properties of iron was carried on in 1996 by Soderlind *et al*[43]. They used an all-electron full-potential linear-muffin-tin-orbital implementation of density functional theory, within the GGA. With this implementation, they reproduce, like Stixrude *et al*[54], the zero temperature equation of state for hcp iron within 1 % and the 14 GPa pressure transition between bcc and hcp. Moreover, they study the stability of bcc, fcc, bct, hcp and dhcp phases as a function of pressure. Of particular relevance is the estimate of the energy difference between the different phases at an atomic volume of 7 $\overset{\circ}{A}^3$, corresponding roughly to the density at the inner core boundary. At this volume, bcc-Fe is mechanically unstable. The phase of lowest energy is nonmagnetic hcp (the stable form of iron at high pressure and room temperature conditions). The other two close-packed phases they consider (fcc and dhcp) are disfavored by $\sim$ 68 meV/atom; the eight-fold coordinated bcc and the ten-fold coordinated bct lie $\sim$ 540 meV/atom above, indicating that only a exceedingly large entropic contribution (ΔS$\sim$ 1 k_B) could stabilize bcc and bct with respect to close-packed phases at high temperature. They also calculate the magnetic moment that survives compression in the various phases. At an atomic volume of 7

$\overset{\circ}{A}^3$, the magnetic moment is totally negligible (¡0.01 μ_B) for all the close-packed phases. For bcc and bct, the magnetic moment is $\sim$0.7 μ_B, indicating some residual magnetism. However, magnetization is expected to decrease strongly with temperature, and the Curie temperature is not likely to be as high as 5000 K[55]. Thus, whatever is the phase of iron at Earth's core conditions, magnetism is likely to play a minor role.

The first attempt to calculate some of the high-temperature properties of iron making large use of first-principle tools, is due to Wasserman *et al*[56]. In their calculation, the electrons are treated within the tight-binding method (whose parameters are fitted to first-principle calculations). The vibrational partition function is estimated by a mean field approximation (the so called cell method [57]) which ignores interatomic correlations. The method can be applied only below the melting transition, where collective motion and diffusion are unimportant. The main contribution of Wasserman *et al* is the estimate of the Gruneisen parameter, the thermal expansivity and of the heat capacity C_v in hcp iron. All these parameters are shown to depend non-trivially on electronic excitations. Moreover, they provide an estimate of the temperature and density along the solid branch of the Hugoniot. Their theoretical values are in good agreement with Brown and McQueen's estimates[13] for both the density and for the temperature.

A similar approach, although based fully on first-principle methods, is used by Vocadlo *et al*[44]. In their work, the vibrational contribution to the free energy is computed within the quasi-harmonic approximation in some of the stable structures at zero temperature (the calculation cannot be performed on bcc, because of its mechanical instability). Within this approximation (that is, however, likely to fail near melting) hcp remains favored with respect to dhcp and fcc at

core pressures and up to 8000 K.

The only first-principles molecular dynamics simulation of iron at Earth's core conditions has been performed so far by A. De Wijs *et al*[49]. Their calculations are based on ultrasoft pseudopotentials of the Vanderbilt type[58]. Electronic exchange and correlation are treated within the GGA of Perdew *et al*[53]. They find out that 3p state partecipate in binding significantly at high pressure, and should be explicitly included in the valence states. However, since their inclusion is computationally very demanding, simulations of liquid iron are performed without explicit treatment of 3p-states. To mimic the effect of 3p states, the authors introduced in the simulation a suitable pairwise ad-hoc constructed potential, thus renouncing to a full first-principle approach. They find that the properties of the liquid phase are sufficiently well converged for increasing system size if simulations are performed on a 64 atoms cell with Γ point sampling of the Brillouin-zone. They thermalize a sample in the liquid state at a temperature of 6000 K and a density of 13.3 g cm^{-3}, corresponding, according to the Anderson and Ahrens equation of state for liquid iron[59], to the density of liquid iron at 330 GPa and 6000 K. After thermalization, they compute the average pressure and the diffusion coefficient D via the Einstein relation. Finally, the viscosity is estimated from D via the Stokes-Einstein relation. The calculated pressure is 358 GPa, 8 % higher than the Anderson value for that density. The viscosity is $\sim$1.5 10^{-2} Pa s, with an estimated uncertainty of a factor of three. This estimate, even if rather rough, is relevant for geophysics, since proposed values for the iron viscosity prior to this calculations spanned more than ten orders of magnitude[60], and the theoretical value is in the low end of the range of previous estimates, with important consequences on geodynamo models[61].

Chapter 2

First-principle calculations.

The approach that is used in this work to compute the properties of iron at Earth's core conditions makes essential use of first-principle tools, since first principle calculations have been shown to provide a very accurate description of static and dynamic properties of a lot of materials, including iron (see Section 1.3).

In this Chapter, after an overview of some concepts that are at the basis of first-principle calculations (in particular, density functional theory, the pseudopotential approach, and Mermin generalization of these theories to metallic systems), we will specify the approximations we use in our first-principle calculations on iron (cutoff in the plane wave expansion, kind of pseudopotential, etc.), discussing the influence these approximations might have on the accuracy of the results. The algorithm employed in our code to minimize the Mermin functional will be briefly described in Appendix A.

In first-principle calculations, the system is represented as a collection of atomic nuclei and electrons, and the forces on the nuclei are obtained by solving the Schroedinger's equation within density functional theory to determine the electronic ground state.

Density functional theory (DFT) is based on a theorem, due to Hohenberg and Kohn[62], showing that the electronic density $n(\mathbf{r})$ and the external potential $V_{ext}(\mathbf{r})$ are univocally determined by each other. Therefore, the electronic density totally defines all the electronic properties of any system, including its total energy.

Thanks to this theorem, the total energy of a system can be written in the form

$$E_{tot}[n(\mathbf{r})] = E_{ext} + \int d\mathbf{r}\, V_{ext}(\mathbf{r})\, n(\mathbf{r}) + E[n(\mathbf{r})] \tag{2.1}$$

where $V_{ext}(\mathbf{r})$ is the external potential (due to the nuclei or any other external source), E_{ext} is the classical energy of the nuclei, and $E[n(\mathbf{r})]$ is a functional of the electronic density, called the *density functional*. $E[n(\mathbf{r})]$ coincides with the expectation value, with respect to the all-electron wavefunctions, of the kinetic energy operator plus the electron-electron interaction.

The density functional can be split in the sum of three terms[63]:

$$E[n] = -\frac{1}{2}\sum_i \langle \Psi_i | \Delta | \Psi_i \rangle + E_H[n] + E_{xc}[n] \tag{2.2}$$

where

$$E_H = \frac{e^2}{2}\int d\mathbf{r}\, d\mathbf{r}'\, \frac{n(\mathbf{r})\, n(\mathbf{r}')}{|\mathbf{r}-\mathbf{r}'|}$$

is the Hartree energy and $|\Psi_i\rangle$ are the orbitals of a fictitious system such that

$$n(\mathbf{r}) = \sum_i |\Psi_i(\mathbf{r})|^2 . \tag{2.3}$$

$E_{xc}[n]$ is called exchange and correlation energy, and is defined by eq. (2.2). The single-particle Hamiltonian whose eigenfunctions are the $|\Psi_i\rangle$-s is called Kohn-Sham (KS) Hamiltonian, and has the form:

$$H_{KS}[n] = -\frac{1}{2}\Delta + V_H[n] + V_{xc}[n] + V_{ext} \tag{2.4}$$

where $V_H[n]$ and $V_{xc}[n]$ are the functional derivative with respect to the density of $E_H[n]$ and $E_{xc}[n]$ respectively. The corresponding Schroedinger equation

$$H_{KS}[n]\,|\Psi_i\rangle = \varepsilon_i\,|\Psi_i\rangle \tag{2.5}$$

is called Kohn-Sham equation.

In order to use equation (2.5) for calculations in real systems, V_{xc} has to be approximated by an explicit function of the electron density. In the so-called local density approximation (LDA)[64], V_{xc} is assumed to be a local operator of the form $V_{xc}(n(\mathbf{r}))$, while in the more sophisticated gradient corrected approximation (GGA)[52, 53], V_{xc} is assumed to depend also on the gradient of the density, i.e. is an operator of the form $V_{xc}(n(\mathbf{r}), \nabla n(\mathbf{r}))$.

Another cornerstone concept in first-principle calculation is the so-called pseudopotential technique[65]. Since core electrons are usually "frozen" in their free-atom configuration, while chemistry and physics are dominated by the behavior of valence electrons, it is customary to map the KS problem (2.5) into an equivalent problem involving valence electrons only and where the valence orbitals are smooth. In particular, a new KS problem of the form

$$H^p_{KS}[n^p]\,|\Psi^p_i\rangle = \varepsilon^p_i\,|\Psi^p_i\rangle \tag{2.6}$$

with $n^p(\mathbf{r}) = \sum_i |\Psi^p_i|^2$ can be defined by the following properties: (i)$\varepsilon^p_i = \varepsilon_i$ for valence electrons in a suitable reference system (usually the free atom); (ii)$\Psi^p_i(r) = \Psi_i(r)$ for $r > r^i_c$ in the same reference system (r^i_c are called cutoff radii) (iii) for $r < r^i_c$ the $\Psi^p_i(r)$ are smooth (and nodeless) functions of the radius; (iv)the pseudowavefunctions $\Psi^p_i(r)$ form an orthonormal set; (v) the charge enclosed within r^i_c for Ψ^p_i and Ψ_i is the same[65, 66].

These properties fully define the operator H^p_{KS} if the reference system and a functional form of the pseudowavefunctions Ψ^p_i for $r < r^i_c$ is chosen. In particular,

H^p_{KS} is usually written in the form

$$H^p_{KS} = -\frac{1}{2}\Delta + V_H\left[n^p\right] + V_{xc}\left[n^p\right] + V_{ps}$$

where $V_{ps}$is a suitable (non-local, in the most general case[65]) operator, called pseudopotential. The set of cutoff radii r_c^i have to be carefully chosen in order to insure both smoothness of the pseudowavefunctions (this would require a large r_c^i) and transferability of the pseudohamiltonian H^p_{KS} to systems very different from the reference system used to construct the pseudopotential (this would require a small r_c^i).

In the rest of this work we will always use the pseudized form of KS Hamiltonian and wavefunction (2.6). Therefore, in the following we will drop the superscript p.

If DFT is applied to a metallic system at finite temperature, the procedure outlined above has to be slightly generalized, in order to allow fractional occupancies of the states as determined by the Fermi distribution. It turns out that the use of a Fermi distribution (or any other "smearing" of the occupations around the Fermi level) improves considerably also the convergence rate of the electronic minimization. In fact, if equations (2.2) and (2.3) are used in a metallic system the number of iterations necessary to converge to a specific precision will increase with the square root of the system size[67], since the energy difference between the last occupied and the first non-occupied orbital is zero for infinite-size systems, and thus it will become progressively harder to determine the correct occupied orbitals. Moreover, any level crossing along a ionic trajectory will cause a sharp change in total energy, with difficulties in integrating the equations of motion.

The inclusion of some unoccupied orbitals above the Fermi level, with suitable partial occupancies, that we will denote by f_i (if a spin-independent form

for the Hamiltonian is assumed, $f_i \in [0, 2]$) ensures instead system-size independence of the minimization efficiency and, moreover, it minimizes the effects of level crossings along the ionic trajectory, smoothing out their effect. At large temperature (T$>$ 1000 K) the electronic temperature (T_{el}) can be set equal to T, while at low T, T_{el} can be kept fictitiously larger than T without affecting the calculated properties[68].

In order to include partial occupancies in a fully consistent manner, the finite temperature version of DFT developed by Mermin[69] has to be used. At a finite electronic temperature T_{el}, the proper variational functional is the free energy of the electrons :

$$F\left(\Psi_i, f_i\right) = E\left(\Psi_i, f_i\right) - k_B T_{el} S_{el}\left(f_i\right) \tag{2.7}$$

where

$$E\left(\Psi_i, f_i\right) = -\frac{1}{2}\sum_i f_i \left\langle \Psi_i \right| \Delta \left| \Psi_i \right\rangle + E_H\left[n\right] + E_{xc}\left[n\right] + \int d\mathbf{r}\, V_{ext}\left(\mathbf{r}\right) n\left(\mathbf{r}\right)$$

is the total energy of the electrons (the electron density is now defined by $n\left(\mathbf{r}\right) = \sum_i f_i \left|\Psi_i\right|^2$) and

$$S_{el}\left(f_i\right) = -\sum_i \left(f_i \ln f_i + \left(1 - f_i\right) \ln\left(1 - f_i\right)\right)$$

is the electronic entropy. The free energy (2.7) has to be minimized with respect to the Ψ_i-s the f_i-s with the constraints of orthonormality of the wave functions and of a constant number N_{el} of electrons. These conditions fully define the occupation numbers f_i as a function of KS energies ε_i (in particular, the occupancies have the Fermi-Dirac form

$$f_i = \frac{1}{\exp\left(\frac{\varepsilon_i - \varepsilon_F}{k_B T_{el}}\right) + 1}, \tag{2.8}$$

where ε_F is the Fermi energy).

In order to allow an efficient minimization of the free energy (2.7) the self-consistency minimization scheme developed by Kresse and Furthmuller[68] has been implemented in a parallel CP code based on a plane-wave expansion of electronic wavefunctions[70]. This method have been shown to outperform, for metallic systems, any other scheme, including direct minimization ones[71][72] and consists in splitting the minimization problem into two sub-problems: an iterative diagonalization of the Hamiltonian at fixed potential and an iterative improvement of the potential, based on a suitable mixing scheme for the charge density. We will describe this method in Appendix A.

We will now discuss some technical details concerning the application of the concepts outlined above to first-principle calculations of iron.

As we recalled in Section 1.3, iron has been the object of extensive studies by the first-principle community, although results concerning its high temperature properties are still incomplete. The approach we use in this work makes use of the detailed know-how that can be extracted from existing experience, in particular concerning the pseudopotential and the kind of exchange and correlation functional that has to be used.

In particular, electronic exchange and correlation are treated using the gradient approximation of Perdew *et al*[52, 53]. This choice for the exchange and correlation functional was shown[54] to provide an excellent agreement with most properties of iron both at low and high pressure, including the room temperature equation of state for bcc and hcp iron, the bcc-hcp transition pressure and the bcc magnetic moment.

Since it was shown by Soderlind *et al*[43] that the magnetic moment in all

close-packed phases of iron at core pressures is almost completely suppressed, the calculations in this work are performed without taking into account electronic spin.

In order to generate the pseudopotential, we have used the procedure developed by Trouiller and Martins[66], since their functional form provides a very reasonable compromise between smoothness of pseudowavefuctions and transferability (in the terms discussed in the preliminary part of this Chapter). Within their approach, we verified that, as already found by A. De Wijs *et al*[49] 3p state polarize significantly at high pressure, and thus these state have to be explicitly included in valence. In particular, failure to include them leads to an overestimation of $\sim$ 80 GPa in the stress at inner core densities. In our approach, also 3s states are included in valence, even if this would not be strictly necessary (their effect might be mimicked, e.g., by using the nonlinear core-corrections[73]) since their inclusion yields a much smoother form for the pseudopotential, and therefore a reduction of the cutoff energy in the plane-wave expansion of KS wavefunctions. The cutoff radii we use are 1.5 au for all the pseudowavefunctions (s, p and d channel). With this choice of cutoff radii, energy differences are converged with respect to the cutoff in the plane-wave expansion of KS wavefunctions at 100 Ryd (e.g., the zero-temperature equation of state for iron with 100 and 150 Ryd coincide within 0.2 % between 0 and 400 GPa).

Also the system-size convergence of our observables has been tested carefully. We obtained that, in agreement with de Wijs *et al*[49], a 64 atom cell with Γ-point sampling of the Brillouin zone is sufficient to reproduce the k-points converged pressures within 0.3 % in all the range of atomic volumes of interest for the Earth's core physics. In Figure 1, the zero temperature EOS for a 64 atoms cell at 100

Ryd cutoff is plotted together with the fully converged (196 special points in the irreducible Brillouin zone and 150 Ryd cutoff) EOS. It is evident that the two equation of state coincide within an error of 0.5 % for every atomic volume.

This theoretical approach gives a low temperature pressure-vs-density curve for hcp iron in excellent agreement with X-ray data[12]. Theoretical and experimental EOS are compared in Figure 1: experimental densities are reproduced with an accuracy between 1.5 %, (around 150 GPa) and 0.8 % (close to the ICB, at 330 GPa).

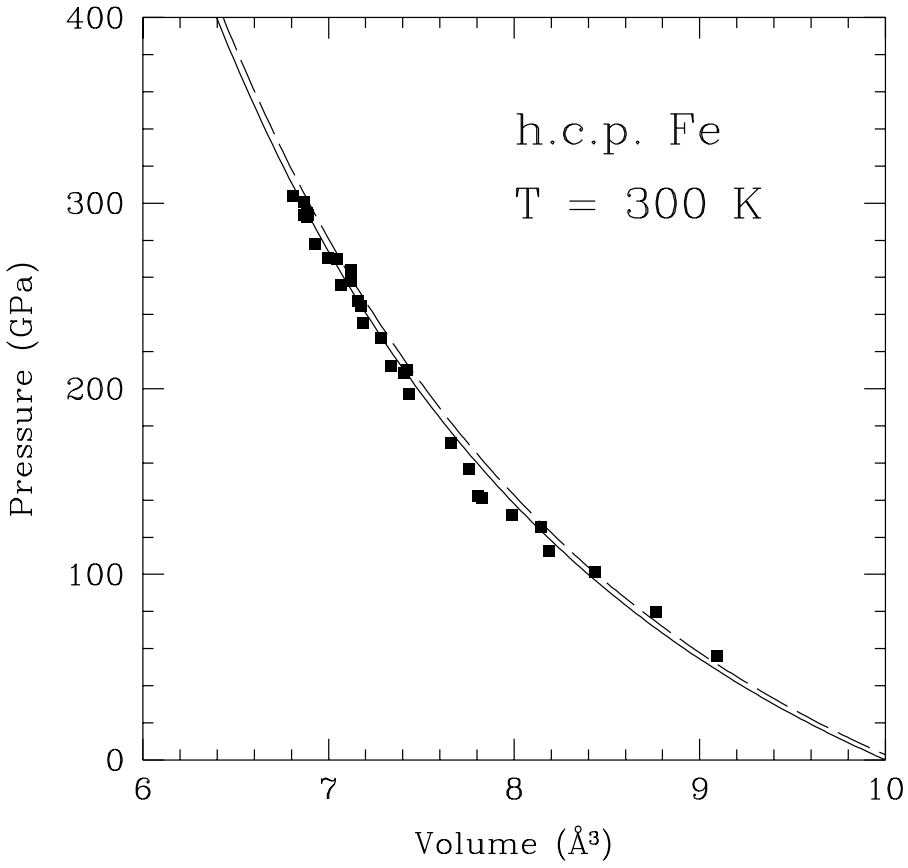

Figure 2.1: Pressure versus Volume equation of state for low temperature hcp iron. Squares: X-ray data at 300 K[12]. Full line: Birch-Murnaghan fit to first-principles results on a 64 atoms cell and 100 Ryd of cutoff in the plane-wave expansion. Dashed line: Birch-Murnaghan fit to first-principle results on a 4 atoms cell with 196 k-points in the irreducible Brillouin zone and 150 Ryd of cutoff.

Chapter 3

The optimal potential method

First-principle calculations have rapidly improved in speed and accuracy, but the range of applicability of these methods still remains limited to systems of relatively small size (from 50 to 500 particles) and short simulation time (a few picoseconds). Although this is sufficient to capture the relevant physics in a large number of cases, a brute-force ab-initio approach can seldom be used to fix the value of most finite-temperature observables at a high level of accuracy, because of unavoidable size effects and because of the poor statistical sampling due to the short simulation time. The case of iron is, in this sense, a good example: the computer time needed to obtain a good quality electronic wave function on a 64 atoms liquid sample is, within the approximations described in Chapter 2, 30 minutes on a 64-node parallel machine in a molecular dynamics run and 3 hours for a ”from-scratch” electronic minimization. It is clear that, in situations like this, even the simple evaluation of an average density by an ab-initio constant pressure run would be almost impossible. The use of Vanderbilt ultrasoft pseudopotential[58] reduces significantly this time, allowing full ab initio evaluation of at least some observables, like the density and the diffusion coefficient, as shown recently

by Gillan *et al* [49]. However, even using Vanderbilt pseudopotentials, a fully ab initio calculation of a melting temperature would be very delicate, because of the great accuracy required in determining free energy differences[74]. Moreover, even the maximum simulation time that can be afforded nowadays ($\sim$ 10 ps [49]) would not allow an accurate estimate of the high temperature elastic constants (see Section 4.4) that are, as we have seen, of great geophysical relevance.

On the other hand, classical interatomic potentials constitute a very powerful tool to perform molecular dynamics simulations on large size systems or for long simulation times, thus avoiding sampling and finite size problems [7].

For the above reasons, it seemed compelling to try to construct a bridge between these two different approaches, making use of the large amount of information that can be obtained by first-principle methods to construct reliable potentials for large-scale computations . This kind of approach (the so called force-matching method, developed by Ercolessi and Adams [75]) has proved quite successful in reproducing the properties of simple metals such as aluminium and lead. The idea underlying this method is to fit the classical potential in order to reproduce not only a set of observables (e.g. the equation of state or the cohesive energy) as in standard potential construction procedures, but also ab-initio forces calculated on a large set of configurations (e.g. a cluster, a surface, a liquid sample).

The drawback of all the approaches based on classical molecular dynamics, including the force-matching method, is the poor capability of classical potentials to describe situations in which relevant changes in the chemistry of the system occur: a *single* classical potential is required to describe the properties of defects, surfaces, clusters, liquids and glasses in a wide range of pressures and temperature. This property, called *transferability*, is considered crucial for the quality

of the potential. To construct a truly transferable potential is, to say the least, a very difficult task, and transferability is often incompatible with the accuracy in the description of a single situation. In practice, even if the potential is fitted to reproduce a large set of properties, its predictivity cannot compare that of an ab-initio calculation, whatever the complexity of the functional form that is used for the classical potential. This has led, in the last ten years, to abandon, whenever possible, of classical potential simulations in favor of the more reliable ab-initio ones.

The idea of the present approach is to *renounce to transferability in favor of accuracy*. This is done by constructing a different classical potential for each distinct physical situation. This approach assumes that the poor capability of a standard classical potential to describe accurately a system (e.g. a liquid at a given pressure and temperature) is due to the requirement that *the same potential* should describe, with the *same* accuracy, many completely different systems (e.g. a liquid at another pressure and temperature, or a surface). If this condition is relaxed, and the classical potential is only required to describe a single system in which no relevant change in electronic structure is expected to occur, the classical potential can, in principle, provide the same information as a full ab-initio run, with an enormous gain in computer time: after the potential is constructed, the full dynamical properties of the system of interest can be easily extracted from extensive classical simulations, without any limitation due to finite-size problems or short simulation time.

In the rest of this work, we will show that it is possible to construct a potential with these properties, that we will call ”optimal potential” (OP), describing iron at a given pressure P and temperature T (also in the presence of melting).

The OPs are constructed, at a given P-T point, by requiring the matching between classical and first-principles forces and stress in selected atomic configurations. This is done in the framework of a suitable iterative procedure, designed in order to reproduce the dynamics of the system at P-T. By definition, this OP will not be transferable to different P-T conditions, where a different potential must be constructed.

This chapter is organized as follows. In Section 1, we introduce the so-called embedded-atom functional form of the potentials that have been extensively employed in classical simulations of metals, and that we used in the potential optimization procedure. In Section 2 the force-matching method, as introduced by Ercolessi and Adams, is briefly reviewed. In Section 3, the iterative procedure for constructing the optimal potential is introduced and discussed. In Section 4, errors due to the OP procedure are estimated by the direct calculation of ab-initio observables in a special case. In Section 5 a method for estimating the melting temperature within the OP procedure is introduced. In Section 6 the OP method is tested by reproducing the thermodynamics of a reference potential by an OP procedure carried out on a classical potential with a completely different functional form.

3.1 Embedded-atom potentials.

As it is well-known, in a metal a substantial fraction of the cohesive energy is due to delocalized electrons. Modeling interatomic forces in a system of this kind leads, in the Born-Oppenheimer approximation, to a classical Hamiltonian depending explicitly on atomic coordinates only, but it is quite unrealistic to model the electron density dependent cohesive term by a simple two body potential[76].

To overcome this problem, several so-called embedded-atom potentials or glue model have been developed. In these potentials the total energy for a monatomic system is assumed to be of the form

$$\begin{aligned} E &= \sum_{k=1}^{N} E_k \\ E_k &= \sum_{j(\neq k)} \left[\frac{1}{2}\Phi\left(R_{kj}\right) + F\left(\rho\left(\{\mathbf{R}_{kj}\}\right)\right) \right]. \end{aligned} \tag{3.1}$$

where N is the number of atoms, $\Phi\left(R\right)$ is a two body potential keeping into account electrostatic interaction and overlap repulsion, ρ is a function of the positions of the neighbors (j) of atom k, mimicking the electronic density experienced by atom k due to the presence of all the other atoms, and F is a suitable non-linear function of ρ. Since $F\left(\rho\right)$ is a non-linear function of the atomic positions, forces arising from the potential (3.1) are in general of the many-body kind. Among the several functional forms for Φ, F and ρ that have been proposed in the literature, we have chosen to use in this work the one proposed by M.I. Baskes [77] (the so-called *modified embedded-atom potential*) because it is the most general and rich we could find (e.g. it includes explicitly angular dependent many body terms) and the one proposed by A.B. Belonoshko and R. Ahuja [78] because it was developed specifically for iron at high P-T conditions. In the rest of this Section, we briefly review these two functional forms.

3.1.1 Modified embedded-atom potentials

In the modified embedded-atom potentials developed by Baskes[77], the two body potential $\Phi\left(R\right)$ is determined by the zero temperature properties of the monatomic solid in a suitable reference structure, i.e. in a crystal structure where detailed informations are available (e.g. the equilibrium structure of the system). In par-

ticular, the two body potential is assumed to be of the form

$$\Phi(R) = \frac{2}{Z}\left[E(R) - F\left(\rho^0(R)\right)\right] \tag{3.2}$$

where Z, $E(R)$ and ρ^0 are the coordination number, the energy per atom (as a function of the atomic distance R) and the density function evaluated in the reference structure. With this definition, the physical properties of the reference structure (in particular the zero-temperature pressure-vs-volume equation of state) are automatically reproduced by (3.1) whatever functional form for F and for the density is chosen. The function $E(R)$ is, by definition, the zero temperature equation of state of the atom. The equation of state is assumed to be of the form

$$\begin{aligned} E(R) &= -E_0\left((1+a)e^{-a}\right) \\ a &= \alpha\left(\frac{R}{R_0} - 1\right) \end{aligned} \tag{3.3}$$

where E_0 is the cohesive energy, R_0 is the zero-pressure nearest-neighbor distance and $\alpha = \sqrt{9B\Omega/E_0}$, where B is the zero pressure bulk modulus and Ω is the zero-pressure volume per atom.

The embedding function F has the form

$$F(\rho) = A\frac{\rho}{Z}\ln\frac{\rho}{Z} \tag{3.4}$$

where the density ρ is of the form

$$\rho = \sqrt{\sum_{l=0}^{3} t_l \rho_l^2} \tag{3.5}$$

The functions ρ_l are dependent upon the relative angular positions of the neighbors of atom k. In particular, if $x_{ij}^{\alpha} = \frac{R_{ij}^{\alpha}}{R_{ij}}$ are the direction cosines, we have

$$\rho_0 = \sum_{j(\neq k)} \rho_0^a(R_{jk})$$

$$\begin{aligned}
\rho_1 &= \sqrt{\sum_{\alpha}\left(\sum_{j(\neq k)}\rho_1^a\left(R_{jk}\right)x_{jk}^{\alpha}\right)^2} \\
\rho_2 &= \sqrt{\sum_{\alpha\beta}\left(\sum_{j(\neq k)}\rho_2^a\left(R_{jk}\right)x_{jk}^{\alpha}x_{jk}^{\beta}\right)^2-\frac{1}{3}\left(\sum_{j(\neq k)}\rho_2^a\left(R_{jk}\right)\right)^2} \\
\rho_3 &= \sqrt{\sum_{\alpha\beta\gamma}\left(\sum_{j(\neq k)}\rho_3^a\left(R_{jk}\right)x_{jk}^{\alpha}x_{jk}^{\beta}x_{jk}^{\gamma}\right)^2}
\end{aligned} \tag{3.6}$$

where $\rho_l^a = \exp\left(-\beta_l\left(\frac{R}{R_0}-1\right)\right)$. The eight parameters β_l, t_l, $l = 0,\ldots 3$ are determined, in Baskes work, from the experimental shear constants and stacking fault energies. At variance with Baskes procedure, these parameters, together with the other four that define a potential, (α, R_0, A and E_0) are determined, in our procedure, by fitting ab-initio forces and stress, as will be discussed in the following sections.

3.1.2 Belonoshko potential

Belonoshko and Ahuja have also developed a potential of the embedded atom form (3.1) for specific application to iron at ICB conditions[78]. The embedded-atom potential they employ is simpler than the one used by Baskes (it does not include angular-dependent many-body terms), but it is of completely different functional form (e.g., the dependence of partial densities on interatomic distance is a power-law, while in Baskes' potential it is exponential). This provided us with the possibility to test the robustness of our procedure, as described in Section 6 of this Chapter.

The pairwise term $\Phi(R)$ is assumed to be of the form

$$\Phi(R) = \left(\frac{A}{R}\right)^n - \frac{C_{vdw}}{R^6} + D\left[\exp\left(-2\alpha\left(R - R_0\right)\right) - 2\exp\left(-\alpha\left(R - R_0\right)\right)\right] \tag{3.7}$$

where the first term is a short-range overlap repulsion, the second term is the van der Waals attraction and the third term is of the Morse form. The many-body term has the form

$$\begin{aligned} F(\rho) &= C\rho^{1/2} \\ \rho_i &= \sum_j \left(\frac{B}{R_{ij}}\right)^m \end{aligned} \tag{3.8}$$

The nine parameters of the potential (A, n, C_{vdw}, D, α, R_0, C, B and m) are optimized, in Belonoshko and Ahuja's original work, by fitting structure, thermal expansion and compressibility of α, γ and ε iron at 300 K and 1 bar, the ε-iron equation of state between 22 and 37 GPa, and by imposing that, at ambient conditions, bcc is the stable form of iron.

3.2 The force-matching procedure.

The most important ingredient of our optimization procedure is a force-matching step, performed on a microscopic configuration $\mathcal{C}$ of N particles on which first-principles stress S_{ij}^{ai}, $i, j = 1, 2$ and forces $\mathbf{F}_i^{ai}$, $i = 1, \ldots, N$ have been computed. The goal of a force-matching step is to generate a potential V_1 that fits accurately these forces[75] and stress. The requirement to fit also the ab-initio stress improved greatly the capability of the fitting routine to find the correct basin of attraction. This is because, for a system with many-body forces, the stress is not a trivial function of the forces like in the two-body case.

The interatomic potential is defined, given its functional form, by its set of parameters $\{\alpha\}$. The force-matching procedure consists of minimizing with respect to $\{\alpha\}$, the distance

$$\mathcal{D}\left(\{\alpha\}\right) = (1 - w_s)\,\frac{\sum_{i=1}^{N} \left|\mathbf{F}_i\left(\{\alpha\}\right) - \mathbf{F}_i^{ai}\right|^2}{\sum_{i=1}^{N} \left|\mathbf{F}_i^{ai}\right|^2} + w_s \frac{\sum_{j,k} \left|S_{jk}\left(\{\alpha\}\right) - S_{jk}^{ai}\right|^2}{\sum_{j,k} \left|S_{jk}^{ai}\right|^2} \tag{3.9}$$

where $\mathbf{F}_i\left(\{\alpha\}\right)$ and $S_{jk}\left(\{\alpha\}\right)$ are the force on atom i and the stress tensor, as obtained with parameterization $\{\alpha\}$ from the classical potential and w_s ($0 < w_s < 1$) weights the relative contributions of forces and stress in the fit. In some special cases (e.g. when a large number of parameters was used) it was necessary to constrain the value of the parameters around some "reasonable" values α_i^0. This was done by including in the distance (3.9) a supplementary term of the form

$$\sum_i w_i \left(\alpha_i - \alpha_i^0\right)^2$$

where w_i are suitable weights.

Given the complication of the functional forms of the classical potentials used, the distance (3.9) has usually multiple local minima. In the present optimization procedure, a large set (~ 100) of potentials which minimize the norm (3.9) is produced by direct Powell minimization starting from randomly chosen initial parameters. Potentials such that $\mathcal{D}\left(\{\alpha\}\right)$ is too large (> 0.05 for the force contribution and > 0.01 for the stress contribution) are immediately discarded. Moreover, a run of ~ 1 picosecond is performed with every potential, and the ones with bad energy conservation are discarded as well. This selection is necessary because no strong bounds on the value of the parameters defining the potentials are introduced, and this can lead, by the minimization procedure, to potentials with sharp derivatives that fit the ab initio forces and stress with a good accuracy, but cannot be used in a long MD simulation.

The required accuracy can be achieved with potentials with different parameters or even different functional forms (in particular of the generalized embedded-atom form or of the Belonoshko form[77, 78]) and we will see in the following section that, if the microscopic configuration where these potentials are optimized is chosen in a suitable manner, all these potentials describe, within a small error, the same thermodynamics.

3.3 Self consistent generation of an optimal potential

The theoretical core of our procedure is the assumption that if potentials generated by a force-matching method *are used in physical conditions that are not too far from the one of the microscopic configuration used to optimize them*, the accuracy of the fit, together with the requirement of conservation of energy, is enough to ensure that any thermodynamic observable, calculated by any of these potentials, will coincide within a small error (depending only on the accuracy of the fit). Potentials satisfying this condition will be called in the following *optimal potentials* (OP), with the understanding that every OP is associated with a particular physical condition, defined, in the case of iron, by pressure and temperature (the possibility of phase transitions at a given pressure and temperature is discussed in detail in Section 5).

An example of the accuracy that can be obtained with our procedure is given in Figure 3.1 (upper part), where the average density of liquid iron at 5500 K and 330 GPa calculated with some OPs is plotted as a function of the constant-pressure MD run time. The potentials are obtained by a force-matching procedure on dif-

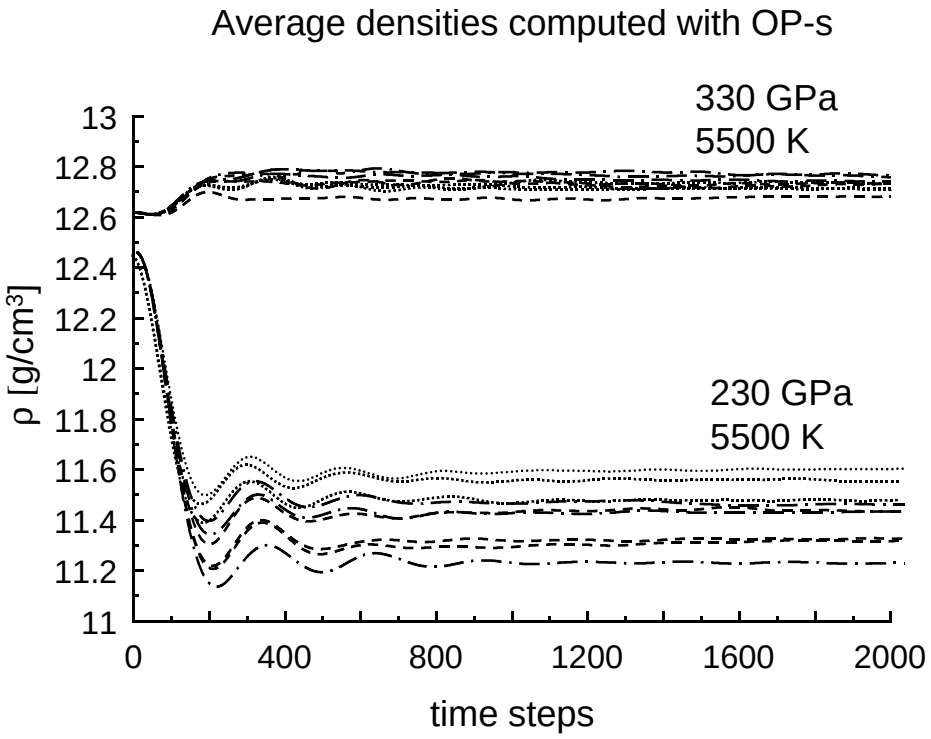

Figure 3.1: Average density as a function of simulation time for twelve potentials optimized at 5500 K and 330 GPa. Each line style corresponds to potentials optimized on different configurations. The simulations are carried out with a 320 atoms cell, at a temperature of 5500 K and at a pressure of 330 GPa (upper part) and 230 GPa (lower part). Note the small spread at 330 GPa and 5500 K (where the OPs have been optimized) and the larger spread for the same potentials used at 230 GPa, indicating non-transferability. (Clearly, at 230 GPa a new set of OPs could be constructed, with spreads as small as the 330 GPa ones.)

ferent microscopic configurations (each line style corresponds to a different microscopic configuration) fulfilling the condition outlined above: the microscopic configurations are, in a sense that we will define more rigorously in the following, at a temperature of 5500 K and at a pressure of 330 GPa. All densities coincide within 0.4 % (the variance is 0.2 % only). The parameters defining the potentials used in Figure 3.1 are reported in Table I (all the potentials are of the modified embedded atom form introduced in Section 3.1.1, with no angular components ($t_l = 0$ for l=1,2,3 in (3.6), with a cut-off of 8 a.u. for the density-dependent part, and of 12 a.u. for the two-body part):

β	$R_0\ [a.u.]$	α	$E_0\ [Ht]$	A
2.786	6.4932	9.5329	0.002195	-6.79499
10.83410	5.2190	3.95768	0.0159	0.3299
-18.6855	6.9456	11.177	0.000481	0.3506
10.2735	5.1973	4.245	0.0635	0.09671
12.2422	5.6778	6.2861	0.01801	0.04013
3.5348	5.7603	7.9766	0.01124	0.35985
9.6745	6.7919	9.6997	0.00216	-0.3952
14.917	6.7673	-3.433	0.0137	0.00551
11.3285	5.6339	9.8181	0.00273	0.3361
11.2928	4.8874	0.0165	0.0388	0.2229
11.043	4.7544	0.0519	0.0379	0.3352
12.6624	5.5988	-0.00261	0.00915	0.1398

Table I: parametrs of the potentials used in Figure 3.1 and 3.2

Despite of the simiarity in the values of the average densities at 330 GPa and

5500 K, the parameters defining the potentials are very different. This similarity in the behavior of optimal potentials extends much further: all the thermodynamical observables (elastic constants, diffusion coefficients, melting temperature, viscosity, etc.), if calculated by these potentials, have approximately the same value(see Figure 3.2 for a comparison of diffusion coefficients calculated with the same potentials and at the same conditions of figure 3.1, and Section 3.5 for a comparison of melting temperatures, heat of crystallization and density jump at melting).

The condition that the potentials have to be used in conditions that are close to the ones of the microscopic configuration on which they have been optimized is crucial: in figure 3.1 (lower part), the density at 5500 K and 230 GPa as calculated with the same potentials used at 5500 K and 330 GPa is reported. The spread in the predicted values of the density is now much bigger (more than 1 %). This shows that the very small spread in density values observed at 330 GPa can be obtained only at a price of a quite weak transferability of the potentials. For this reason, the potentials have to be used only in a small neighborhood of the physical conditions where they are optimized (experience has shown that our potential are transferable, with the accuracies we require, within a window of ~ 30 GPa in pressure and ~ 500 K in temperature around the P-T point where the potential is fit).

There are two different methods to ensure that a microscopic configuration is a ”good representation” of a given thermodynamic state (defined, in our case, by pressure and temperature). The first one is to perform a constant P-T ab-initio molecular dynamics run on the system of interest and optimize the potential *after equilibration*. This possibility, although very reliable and feasible for a large class of system, is not realistic for iron, given the cost of performing a single molecular

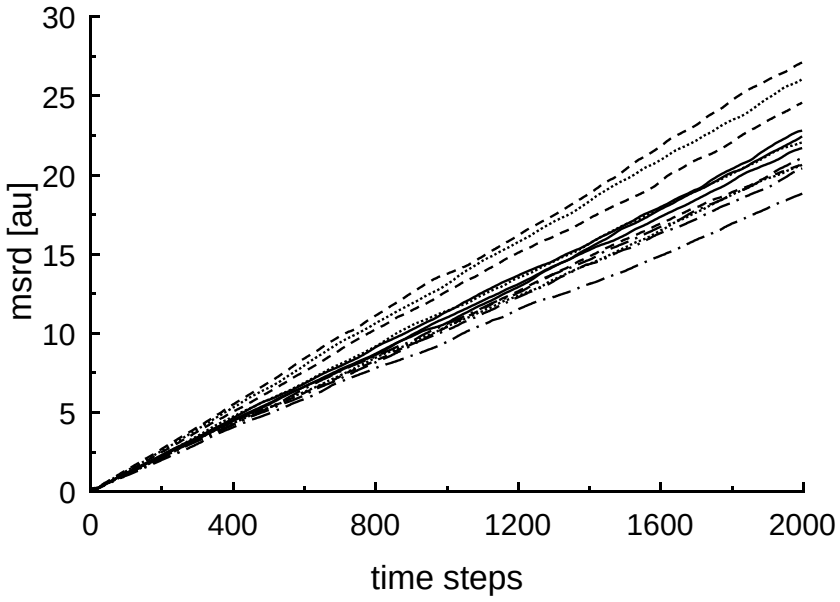

Figure 3.2: Mean square root displacement (msrd) as a function of simulation time for twelve optimal potentials (the same of Figure 3.1). msrd are averaged on 20 runs carried out with 320 atoms cells, at a temperature of 5500 K and at a pressure of 330 GPa. A time step corresponds to 0.967 fsec. The observed spread between the curves of msrd-vs-time corresponds approximately to a 25 % of uncertainty in the diffusion coefficient.

dynamics step.

The second possibility is to perform an iterative procedure, in which the distance from convergence is defined by the variation, on iteration, of a *control variable*, i.e. a macroscopic observable different from the ones fixing the thermodynamic state of the system (pressure and temperature). In the case of iron, we have chosen the density ρ at P-T as the control variable.

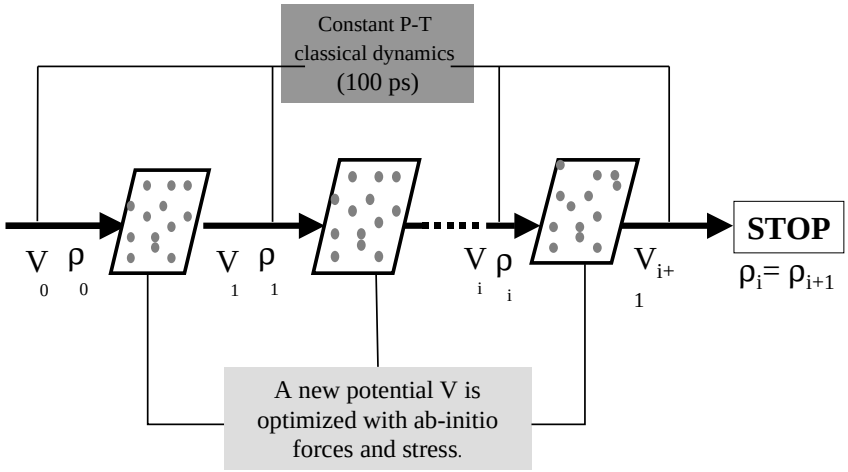

Figure 3.3: Iterative procedure for constructing optimal potentials at P-T

The iterative procedure is the following (see also figure 3.3). A trial many-body interparticle potential V_0 [77, 78] is used to produce a classical trajectory for a (small) number N of particles in the isothermal-isobaric ensemble at P-T; the density ρ_0, averaged on this trajectory, is calculated. In the resulting configuration $\mathcal{C}_1$ first-principles stress and forces are computed, and a new potential V_1 is generated by a force-matching procedure[75] on this configuration. The configuration is then evolved with the new potential V_1, still at P-T, and a new average density ρ_1 is calculated. If $|\rho_1 - \rho_0|/\rho_0$ is small (less than 5×10^{-3} in the case of iron) the classical potential V_1 generated in this way is accepted as optimal at the given P-T

conditions, otherwise the procedure is iterated, generating in this way a sequence of potentials V_i, each of them defined by a functional form and a set of parameters.

As stated above, V_i is not unique, since other potentials differing in the choice of the parameters and/or of the functional form can satisfy the required fitting accuracy on forces and stress (an example is provided by the potentials in Table I). All the potentials V_i can be thought of as belonging to a class $\{V_i\}$, defined completely by the configuration $\mathcal{C}_i$ and by the accuracy of the fit. Potentials belonging to the same class produce (at the same P-T conditions), the same density, within an error of $\Delta\rho$, and the same value for a lot of other thermodynamic observables (an example of this property is given in figure 3.1, in which every line style corresponds to a different class and $\Delta\rho/\rho \sim 0.4$ %, and in figure 3.2). The iterative procedure is stopped if the classes of potentials $\{V_i\}$ and $\{V_{i+1}\}$ produce the same density within 0.5 %. This implies that the two classes describe, with a rather good approximation, the same thermodynamics.

It should be noticed that the number of iterations that had to be carried out to optimize potentials for iron was in fact seldom larger than three: the more the thermodynamics of the system was becoming clear, both from previous calculations, and from comparison with experimental data, the easier it was to guess a reasonable trial density at P-T, thereby speeding up the procedure.

It also has to be underlined that the potentials are optimized using rather small cells (the number of atoms that can be treated in fully ab initio calculations is limited) while thermodynamic quantities, such as the melting temperature, are most of the times computed on much bigger cells. This provides accurate results only if the range of interatomic forces is smaller than the size of the cell of the ab initio calculation. In this work, ab initio quantities are computed on 64 atoms

cells, thus at least 3 nearest neighbor shells are included for every atom in the simulation. We believe the error induced by this approximation is much smaller than other errors implicit both in the procedure and in the ab-initio calculation itself (e.g. poor k-points sampling).

To give an idea of the overall efficiency of this method, if applied to iron at high P-T conditions, the total number of ab-initio minimizations on independent 64 atoms configurations that it was necessary to perform in order to characterize the full high P-T phase diagram of iron is ~ 100. The equivalent number of time steps that we could have afforded in a single "brute force" ab-initio molecular dynamics run is ~ 600, i.e. less than 2 ps of trajectory (with a 40 a.u. time step). This time would have been hardly sufficient to thermalize the system *at a single* pressure and temperature.

3.4 Estimation of errors due to the optimized potential procedure.

A very important property of potentials optimized by a force matching step is that the more the optimization procedure has been accurate, the more the Born-Oppenheimer surface of the ab-initio potential is locally tangent to the constant energy surface of the classical potential (in particular, if the norm (3.9) is zero, the two surfaces coincide in a neighborhood of the configuration $\mathcal{C}$). Of course, this is a local property, and nothing, except for the functional form of the potential, constrains the two surfaces to remain close to each other far from $\mathcal{C}$. Nevertheless, it is interesting to study the differences and similarities of the two dynamical systems (defined by the ab-initio and by the classical potential respectively) far

from $\mathcal{C}$.

Let us denote by (p, q) the canonical variables defining the system, by $T(p)$ the kinetic energy, by $V_{ai}(q)$ the ab-initio potential energy, and by $V_{op}(q)$ the potential energy of the classical optimized potential. By a molecular dynamics simulation, the trajectory of the system defined by the optimal potential starting from the configuration $\mathcal{C}$ can be computed. We denote this trajectory by

$$(p_t, q_t). \tag{3.10}$$

This trajectory conserves the initial energy, i.e.

$$E_{op}(t) = T(p_t) + V_{op}(q_t) = T(p_0) + V_{op}(q_0)$$

but, of course, it does not conserve the ab initio energy i.e.

$$E_{ai}(t) = T(p_t) + V_{ai}(q_t) \neq T(p_0) + V_{ai}(q_0)$$

A quantitative measure of the quality of the optimized potential is given by the behavior with time of the distance between the two surfaces far away from $\mathcal{C}$ i.e. of the quantity

$$\begin{aligned} \Delta(t) &= [E_{ai}(t) - E_{ai}(0)] - [E_{op}(t) - E_{op}(0)] = \\ &= [V_{ai}(q_t) - V_{ai}(q_0)] - [V_{op}(q_t) - V_{op}(q_0)]. \end{aligned}$$

$\Delta(t)$ has to be very small for a very good quality OP: if the OP is able to reproduce exactly the first-principle forces and stress, the OP conserves also the ab-initio energy and $\Delta(t) = 0$. The average value of $\Delta(t)$, if compared to the error that can be accepted on thermodynamic observables, is a very reliable measurement of the predictivity of the optimized potential. To give an example of the level of accuracy that can be obtained with our procedure, in figure 3.4 we plot

$V_{op}(q_t) - V_{op}(q_0)$ and $V_{ai}(q_t) - V_{ai}(q_0)$ as calculated on 12 different configurations 200 time steps far apart along the classical molecular dynamics run. The OP has been optimized on the first configuration (at 200 GPa and 4100 K, on solid iron). The optimal potential is able to reproduce the variations of V_{ai} with an accuracy better than 100 K, when the variation of the potential energy is larger than 1500 K, i.e. the value of $\Delta(t)$ is smaller than 100 K in all the twelve configurations where first-principle energy is calculated. Moreover, the errors on $\Delta(t)$ tend to compensate, so that its average value is smaller than 30 K .

The *internal energy* of the system $\langle V_{ai}(q)\rangle$ is estimated, within the optimal potential procedure, by

$$U = V_{ai}(q_0) - V_{op}(q_0) + \langle V_{op}(q)\rangle \tag{3.11}$$

Thus $\langle\Delta\rangle = U - \langle V_{ai}(q)\rangle$ is an estimate of the error on U.

The order of magnitude of energy differences that are of interest in the system is given, e.g., by the heat of crystallization. This is, for iron at ICB conditions, approximately 5000 K, as we shall see in the following. Thus, the accuracy observed in Figure 3.4 is sufficient to fix energy differences within a precision of $\sim$ 1 %.

The same kind of comparison can be carried out for the stress evaluated along the classical molecular dynamics run. In particular, the average ab-initio stress $\langle S_{ai}(q)\rangle$ is estimated, in the optimal potential procedure, by

$$S = S_{ai}(q_0) - S_{op}(q_0) + \langle S_{op}(q)\rangle \tag{3.12}$$

where S_{op} is the stress evaluated by the optimal potential. In Figure 3.5, the trace of $(S_{op}(q) - S_{op}(q_0))$ and of $(S_{ai}(q) - S_{ai}(q_0))$ are plotted for the twelve configurations of Figure 3.4. The quantity defining the predictivity of the optimal

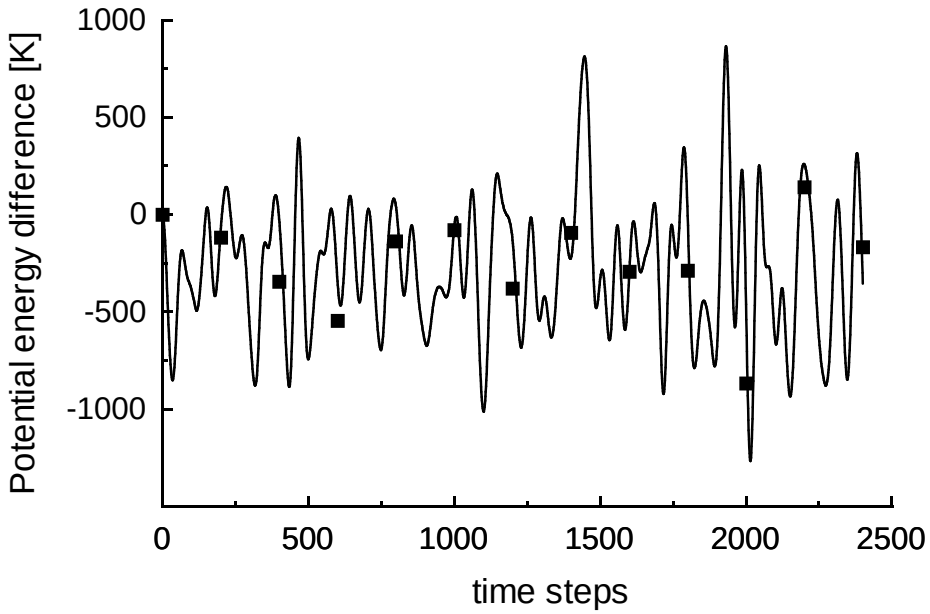

Figure 3.4: Comparison between potential energies as obtained by an optimal potential and by ab-initio calculations, along a single OP trajectory. Full line: potential energy in a classical run performed with an OP generated at 200 GPa and 4200 K. Squares: first-principle total energy, referred to the $t = 0$ configuration, computed at intervals of 200 time steps along the OP trajectory.

potential is the difference between the two OP and the first-principle stress. The OP is able to reproduce the first-principle values with an accuracy better than 1 GPa in all the twelve configuration, The average value of these errors is $\sim$ 0.3 GPa, corresponding once again to $\sim$50 K (VΔP) on an energy scale. The error in atomic volume V due to this error on the stress can be estimated by $\delta V \simeq V\frac{\delta S}{B}$, where B is the bulk modulus (at 200 GPa the bulk modulus B is $\sim$ 1000 GPa), thus the error $\delta V/V$ is less than 0.5 %.

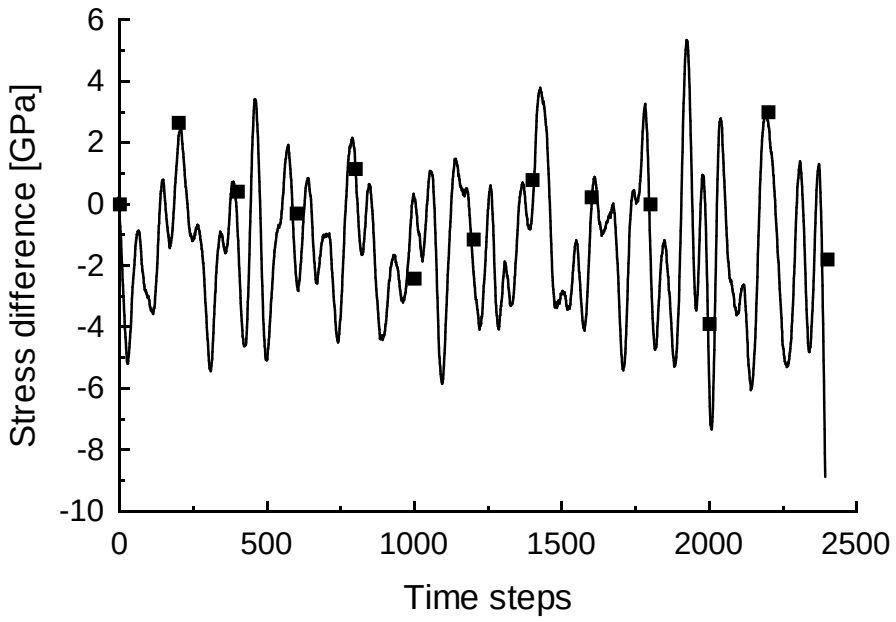

Figure 3.5: Comparison between stress as obtained by an optimal potential and by ab-initio calculations, along a single OP trajectory. Full line: trace of the stress tensor in a classical run performed with an OP generated at 200 GPa and 4200 K (same run as in Figure 3.4). Squares: first-principle stress, referred to the $t = 0$ configuration, computed at intervals of 200 time steps along the OP trajectory.

Expressions like (3.11) and (3.12) for the internal energy and average pressure are very powerful, since they allow the estimation of the thermodynamic averages $\langle V_{ai}(q)\rangle$ and $\langle S_{ai}(q)\rangle$ with a very small error and at the cost of a single evaluation of ab-initio quantities (in the configuration $\mathcal{C}$). If the observable that has to be computed depends on the size of the system, or if its evaluation requires classical MD runs with a number of particles much larger than ~ 100, the expressions (3.11) can be generalized as follows. If N_{ai} is the number of particles in the configuration $\mathcal{C}$ (where ab-initio quantities are computed) and N_{cl} is the number of particles used in the classical simulation, we have

$$\frac{\langle V_{ai}(q)\rangle}{N_{cl}} \simeq \frac{V_{ai}(q_0) - V_{op}(q_0)}{N_{ai}} + \frac{\langle V_{op}(q)\rangle}{N_{cl}}$$

where the averages are taken over trajectories of N_{cl} particles. This expression easily allows a size-scaling analysis of the observables, but, as we already discussed, it is correct only if the range of the forces is smaller than the size of the cell used to optimize the potential.

3.5 Calculation of melting temperature by optimal potential technique.

As is well known, the calculation of the melting temperature is a non-trivial task even for systems where a good statistical sampling can be afforded[74].

In this Section, we describe a method for estimating the melting temperature T_m through the optimal potential technique. Since T_m is not known a priori, the OP technique cannot be applied straightforwardly like for the internal energy(3.11). In fact, the temperature is, together with pressure, the variable fixing the thermodynamic state of the system. This imposes the use of a further

iterative procedure, leading, at the end, to a classical potential that is *optimal at* P-T$_m$ *and whose melting temperature is exactly* T$_m$. This last property defines the melting temperature within the optimal potential procedure.

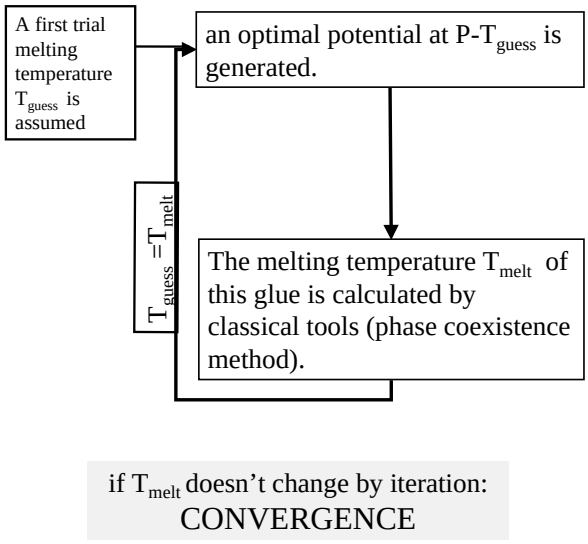

Figure 3.6: Iterative procedure for calculating the melting temperature at a given pressure by the optimal potentials.

The iterative procedure (also described in Figure 3.6) is the following. Starting from a trial T^0_m, an OP class is determined at P,T^0_m and the average melting temperature T^1_m of these potentials is computed; a new OP class is then determined at P-T^1_m and the procedure is iterated until T$^{i+1}_m \simeq$ T^i_m. At the end of the iterative procedure, all the values for the melting temperature calculated within a class of OP-s turned out to coincide within ± 100 K, that gives the estimated error on T$_m$ due to the OP procedure. In Table II the melting temperatures of potentials optimized at 330 GPa and at the temperature reported in the column T_{opt} are reported , together with the density jump at melting $\Delta\rho/\rho$, the density of the liquid ρ_l at melting and the heat of crystallization ΔH. The potentials optimized at 5400 K

are at convergence with respect to the iterative procedure described in this Section. The spread of the observables ($\Delta\rho/\rho$, ρ_l and ΔH) within the class of converged potentials defines the uncertainty due to the OP procedure.

It should be noted that it is not *a priori* obvious that the same classical potential can describe with good accuracy both the solid and the liquid, even if they are at the same temperature and pressure, and a reliable calculation of the melting temperature is possible only if *both the solid and the liquid* are described with equal accuracy. This requirement imposed a further test of our method. In fact, the optimization procedure can be carried out, in the vicinity of the melting, both on liquid and solid trajectories. The first six potentials in Table II have been optimized on liquid samples only, while the last 6 on solid samples only. Finally, the thirteenth potential has been optimized using both liquid and solid configurations. The average T_m of the set of potentials optimized on liquid samples (keeping into account converged potentials only) is ~ 100 K higher that the average value for set optimized on solid samples. This difference might indicate a possible change in the electronic structure between solid and liquid iron at ICB conditions that can be described neither by classical potentials of the functional form [78] and [77] nor, probably, of *any* functional form. Since 100 K is a rather small error (of the order of magnitude of the spread in T_m within an OP class) we accepted our results on melting temperature as sufficiently reliable. Nevertheless, this discrepancy is very likely to become more important in systems where relevant changes in electronic structure occur at melting (like silicon), and the errors associated with the OP method in these systems is likely to be larger.

In brief, the total estimated error on T_m of iron at ICB conditions (± 100 K) reflects variations of T_m obtained with different OP-s and this small discrepancy

between OP-s optimized on solid and liquid samples. Errors due to the calculation of T_m using each classical potential (see the following of this section) were checked to be $\ll 100$K, as is typical for these kind of calculations.

Potential fit to:	T_{opt}[K]	T_m[K]	ρ_l[g/cm^3]	$\Delta\rho/\rho \times 100$	$\Delta H \times 10^6$J/Kg
liquid	5700	5605	12.733	1.45	.74
liquid	5700	5200	12.677	1.6	.65
liquid	5700	5490	12.722	1.44	.67
liquid	5400	5280	12.701	1.62	.65
liquid	5400	5385	12.704	1.54	.69
liquid	5400	5437	12.737	1.64	.69
solid	5200	5547	12.765	1.36	.74
solid	5200	5685	12.748	1.87	.76
solid	5200	5300	12.757	1.62	.73
solid	5400	5510	12.714	1.78	.71
solid	5400	5470	12.715	1.85	.7
solid	5400	5450	12.731	1.82	.69
liquid+solid	5400	5490	12.707	1.58	.68

Table II: Melting temperature, density of the liquid at melting, density jump at melting and heat of crystallization at 330 GPa computed with OPs optimized on liquid samples only, solid samples only and both liquid and solid samples at 330 GPa and at a temperature T_{opt}.

The solid-liquid coexistence method was used as the melting criterion on each classical potential[79]. This method consists in performing a simulation of a large

(up to 6000 particles) system, with a sample that is prepared, by a suitable constrained dynamics, half molten and half frozen (as can be checked from the behavior with time of displacements of the particle from the initial positions). If microcanonical MD is used, and if the initial temperature is not too far from T_m, the sample tends to stabilize at the melting temperature: e.g., if the initial temperature is higher than T_m, some of the frozen part will melt, decreasing the temperature proportionally to $\frac{N_m}{N} H_m$, where H_m is the heat of crystallization and N_m/N is the fraction of the sample that melts during the simulation.

Since freezing and melting are accompanied by substantial changes of volume, it is essential to perform the simulations at constant pressure. In the solid-liquid coexistence method, liquid and a solid are piled up along the z-axis of a cell, and the cell dynamics is required to conserve this symmetry. Since the interface between liquid and solid is orthogonal to the z axis, such an inhomogeneity of the sample might cause instabilities if the cell were to be evolved by a standard Parrinello and Rahman dynamics[80]. Our simulation are thus carried out with a first (quite short) thermalization run at a temperature estimated to be close to T_m, leaving the z axis free to evolve with a Parrinello and Rahman-like dynamics. This process equilibrates the liquid part of the sample at the required pressure, but some residual xy-stress remains in the solid part. A microcanonical run is then carried out with a Parrinello Rahman dynamics for the z axis and, independently, on the x-y plane (this is achieved by setting to zero the zx and zy components of the stress). In this way, the solid fraction of the sample is also free to relax to zero-stress conditions. By this procedure it is possible to estimate T_m within an error of 50 K using a single run of ~ 30 ps if the initial guess on T_m is correct to within 300 K (for a system with $\Delta \mathrm{S} \sim \mathrm{k}_B$ like iron at ICB).

An additional feature of the solid-liquid coexistence method is that by this approach it is possible not only to compute the melting temperature, but also to distinguish the most stable solid phase before melting. If, e.g. a sample of liquid in equilibrium with a solid phase A stabilizes at 1000 K, while a sample of liquid in equilibrium with a solid phase B stabilizes at 1100 K, we can conclude that the stable phase of the system before melting is B. If A is the stable form of the system at T=0 K, this indicates the existence of a solid-solid phase transition from A to B below melting. With this approach we to checked the relative stabilities of bcc and hcp iron at ICB conditions (see the following Chapter).

3.6 Test of the method by a classical reference potential.

The OP method has been tested using a classical ”reference potential” with the functional form (3.7) (3.8) playing the role of the first-principle potential, and by optimizing, using our procedure, a potential of generalized embedded-atom form (3.2), (3.3) (3.4)in order to reproduce thermodynamical quantities provided by the reference potential, including the melting line.

At variance with the case in which the reference potential is the first-principle potential, in this case the predictions of the method can be directly compared with the exact values of the observables, as computed by molecular dynamics run performed with the reference potential.

The potential parameter that have been chosen for the reference potential are

$$\begin{array}{lll} A = 1.9779 \text{ au Ht}^{1/n} & D = 2.389\ 10^{-2}\text{Ht} & \alpha = 1.018\,\text{au} \\ B = 6.1287\text{au} & n = 6 & R_0 = 2.004\text{au} \\ C = 1.1301\ 10^{-2}\,\text{Ht} & m = 8.5 & C_{vdw} = 9.6856\,\text{Ht au}^6 \end{array}$$

Potentials of the functional form (3.2), (3.3) (3.4) are able to fit forces and stress generated by potentials of the form (3.7) ((3.8) with approximately the same accuracy that can be obtained if first-principle forces and stress are fitted.

As a first check, we repeated the comparison performed in Section 3.4 between observable directly calculated with the reference potential (the first-principle potential in Section 3.4) and the OP. Since the reference potential is in this case a classical potential, we could calculate and compare the observables (energy and stress) on a full run and not only on few configurations as in Section 3.4. The behavior observed in Figure 3.4 and Figure 3.5 is fully recovered, i.e. the OP is able to reproduce the potential energy and the stress as computed with the reference potential with an accuracy better than 100 K and 1 GPa respectively (see Figure 3.7). The behavior of $\Delta\,(t)$ as a function of time along the OP run is also reported in Figure 3.7 (lowest part). This last curve is a very reliable measurement of the quality of the OP since it indicates that the reference potential total energy is almost exactly conserved (within $\sim$ 100 K) in the MD run performed with the OP.

Finally, we calculated some thermodynamic quantities provided by the reference potential by the OP technique described in this Chapter. The accuracy obtained is very good both for equilibrium and dynamic properties. E.g., the melting temperature of the reference potential at 330 GPa is 5600 K. This value is reproduced by the optimal potentials within 50 K. The density jump at melting at 330

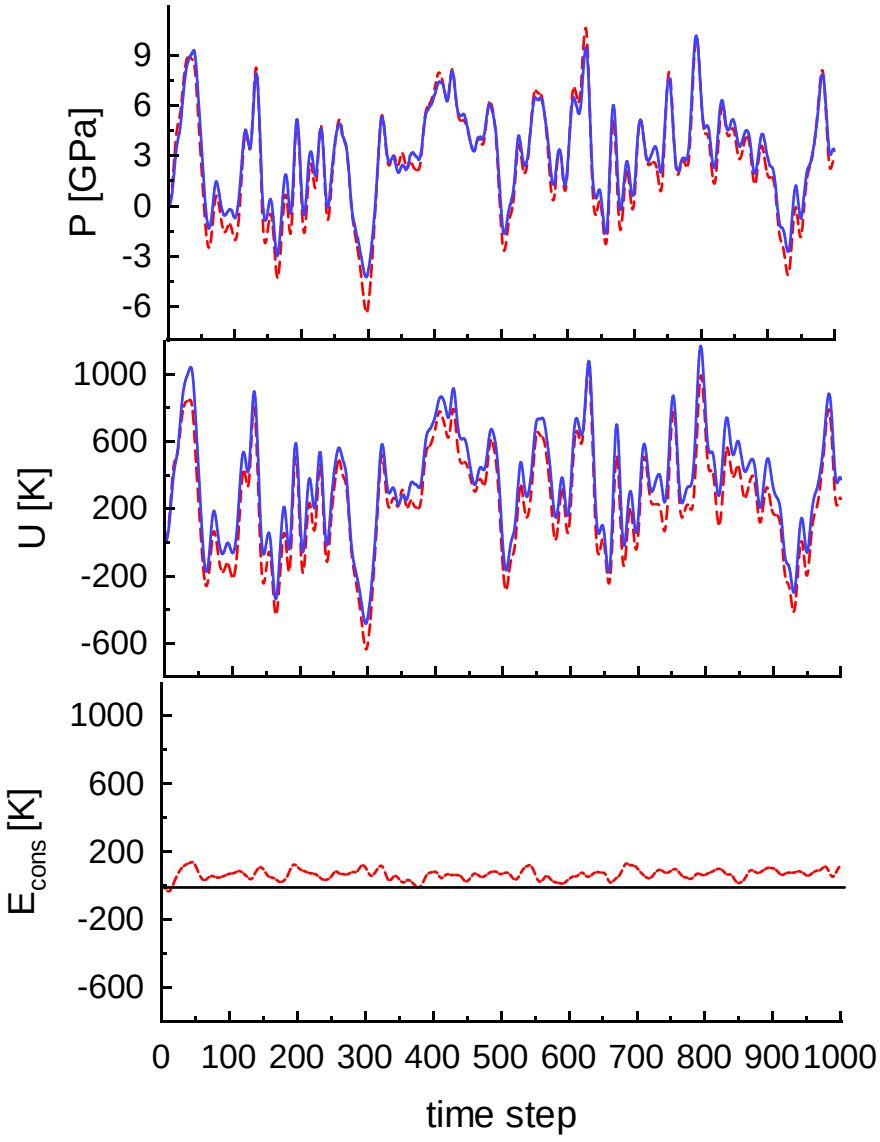

Figure 3.7: Comparison between calculations performed with the reference potential and with an optimal potential. Dotted line: reference potential (of the form (3.7) and (3.8). Full line: optimal potential (of the form (3.2),(3.3), (3.4)). Higher part: trace of the stress tensor in a run performed with 64 particles at 330 GPa and 5500 K. Middle part: potential energy in the same run. Lower part: total energy.

GPa, averaged on six different OPs, is 1.79 (± 0.1) %, only .11 % higher than the exact value (1.68 %).

Chapter 4

Calculated properties of iron at Earth's core conditions

The method outlined in the previous chapter is now applied to the calculation of the properties of iron at high pressure conditions. Some of the quantities that are calculated here, in particular the room temperature elastic constants and the shock-wave compression equation of state and sound velocities, can be directly compared with experiments, thus supporting the validity of the method. In other cases (e.g. for the melting temperature), a comparison with experiments, where available, is more delicate, due to the large spread of experimental data. Our predictions will be discussed in details also concerning their geophysical implications.

This Chapter is organized as follows: in Section 4.1, experimental and theoretical room temperature elastic constants are compared and it is shown that our method is able to reproduce the experimental values within few percent of accuracy. In Section 4.2, we discuss the application of the method to the calculation of the melting line of iron between 100 GPa and 330 GPa. Our predictions are

shown to be in good agreement with DAC measurement, up to the highest pressure where they are available, but not with the values extracted from shock-wave measurements. Results on other observables related to the melting, such as the heat of cristallization and the density jump, are also presented and discussed in terms of geophysical implications. The density of liquid and solid iron at melting and at 330 GPa, i.e. at the inner core boundary pressure, is computed in Section 4.3 (we already recalled that the difference between this value and the density of Earth's core at the ICB is a quantity of great geophysical relevance, since it constrains the amount of light elements in the core). Theoretical values for the bulk and the shear velocities at ICB conditions are computed as discussed in Section 4.4, where we show that an inner core entirely composed of hcp iron and a minor amount of impurities is perfectly compatible with seismological data. Finally, the theoretical shock-wave compression line, the so called Hugoniot, is calculated and compared with experiments in Section 4.5.

4.1 Room temperature elastic constants

Room temperature elastic constants have been recently measured up to 210 GPa in a work by Mao *et al* [12], and have been recently calculated with ab-initio methods [23]. This provided us the possibility to test the OP method, by comparing our results with well-settled experimental measurements and independent theoretical estimates.

The low temperature elastic constants are obtained in our procedure by the finite-strain method [23], thus neglecting differences between 0 K and 300 K values, on a potential optimized at 210 GPa and 300 K, i.e. at the highest pressure reached in the experiment. At such low-temperature conditions, the inclusion

of angular-dependent many-body forces in the functional form for the potential proved essential to produce a satisfactorily fit of ab-initio forces and stress (in particular, the inclusion of these terms is essential to reproduce the observed non-ideal c/a ratio). As the temperature increases, the inclusion of angular dependent components does not significantly improve the accuracy of the fit. Therefore, close to the melting line, angular components can actually be neglected.

In the finite-strains method, elastic constants are computed as the second derivatives of the energy (computed for fully relaxed atomic positions within the cell) with respect to the strain tensor ε_{ij}. In particular, we have[81]

$$C_{ij} = \frac{1}{V}\frac{\partial E}{\partial \epsilon_i \partial \epsilon_j} \tag{4.1}$$

where ϵ_i is directly linked to the strain tensor ε_{ij} by the relations

$$\epsilon_i = \varepsilon_{ii} \text{ for } i = 1, 2, 3$$

$$\epsilon_4 = \varepsilon_{23}, \ \epsilon_5 = \varepsilon_{13} \ \epsilon_6 = \varepsilon_{12}.$$

In the hexagonal lattice, there are five independent elastic constants: C_{11}, C_{12}, C_{33}, C_{44} and C_{13}. Other elastic constants can be obtained as linear combinations (e.g. $C_{66} = C_{11} - C_{12}$)[81].

The five independent elastic constants can be calculated by applying five independent strains and estimating the second derivative of the energy with respect to the applied strain. E.g., if the strain is

$$\varepsilon(\delta) = \begin{pmatrix} 0 & 0 & \delta \\ 0 & \delta^2(1-\delta^2) & 0 \\ \delta & 0 & 0 \end{pmatrix}$$

the change in total energy is,

$$E(\delta) = E(0) + 2\,C_{44} V \delta^2 + \mathcal{O}\left(\delta^4\right)$$

and this gives us C_{44}.

The low-temperature elastic constants, as calculated by our procedure, are shown in Table I. They compare satisfactorily with full ab-initio calculations[23] and also with recently revised DAC data[5]. The error on these quantities due to OP procedure (again estimated as the spread of the quantity within the single OP class) is 5 %.

Bulk and shear modulus are computed as Voigt averages[3], i.e. are given by

$$B_v = \frac{1}{9}\left(4C_{11} + C_{33} + 4C_{13} - 4C_{66}\right) \tag{4.2}$$

$$S_v = \frac{1}{15}\left(C_{11} + C_{33} - 2C_{13} + 5C_{44} + 6C_{66}\right) \tag{4.3}$$

The error on B_v and S_v is $\sim 1\%$, smaller than the error on single elastic constants (possibly errors on single elastic constants tend to compensate in isotropic averages).

	Elastic constants of h.c.p. Fe at 300K and 210 GPa						
	C_{11}	C_{12}	C_{33}	C_{13}	C_{44}	B_v	S_v
Th: opt. pot.	1554	742	1796	820	414	1074	414
Th: ab-initio [23]	1697	809	1799	757	421	1085	445
Exp: D.A.C. [5]	1533	846	1544	835	583	1071	396

4.2 The melting line of iron

The melting temperature of iron at 330 GPa is a quantity of great geophysical interest, since it constrains the temperature of the Earth at the ICB.

The full melting line of iron between 100 GPa and 330 GPa was computed with the method outlined in Section 3.5. As already discussed, this method provides an estimate of T_m with an error of $\pm$100 K, as estimated by the spread of

T_m within a class of optimal potentials. In principle, since the stable phase of iron at ICB conditions has not been unambiguously determined, one should compute the melting temperature of all the possible phases, the stable one being the one that melts at the highest temperature. In this work, only hcp and bcc are explicitly taken into account. hcp is considered in the literature as the most probable candidate phase for iron at ICB conditions [33]. Iron in fact remains in the hcp phase (ε-Fe) at room temperature up to very high pressure (more than 400 GPa [43]). bcc, even if it is calculated to be mechanically unstable at 300 GPa and low temperature [43], has been proposed several times as the high temperature phase of iron 300 GPa [25, 42]. We found that bcc iron melts ~ 300 K below hcp iron at 330 GPa, and $\sim$ 500 K below at 150 GPa. [1] Since these numbers are well above our accuracy on T_m, our calculations confirm that hcp is favored with respect to bcc at ICB conditions. Concerning other close packed phases suggested in the literature (fcc, dhcp, etc.) it has to be noticed that free energy differences between hcp and these phase are likely to be smaller than the accuracy of the OP method. For example, the difference in the melting temperature of hcp and fcc iron at 330 GPa as found by Poirier with thermodynamical arguments is 100 K (in favor of hcp). This free energy difference is very small and it is comparable with the error of the OP procedure. Thus, we decided not to consider the possibility of other close packed structures but hcp even if these phases have been proposed several times (in the case of dhcp with some experimental evidence in favor [45, 47], as

[1] We also calculated the high-pressure elastic constants of bcc iron close to melting, obtaining (by the technique described in Section 4.4) very low values for the shear elastic constants. Given the accuracy that can be obtained with our method on these observables (see Section 4.4), a zero or negative value cannot be excluded. This might indicate that bcc might be, also at high temperature, mechanically unstable with respect to more close-packed phases, such as bct and fcc.

we recalled in Section 1.2.3) with the assumption that the difference will be tiny not only for the melting temperature, but also for other thermodynamic properties of geophysical interest, such as the heat of crystallization and the densities.

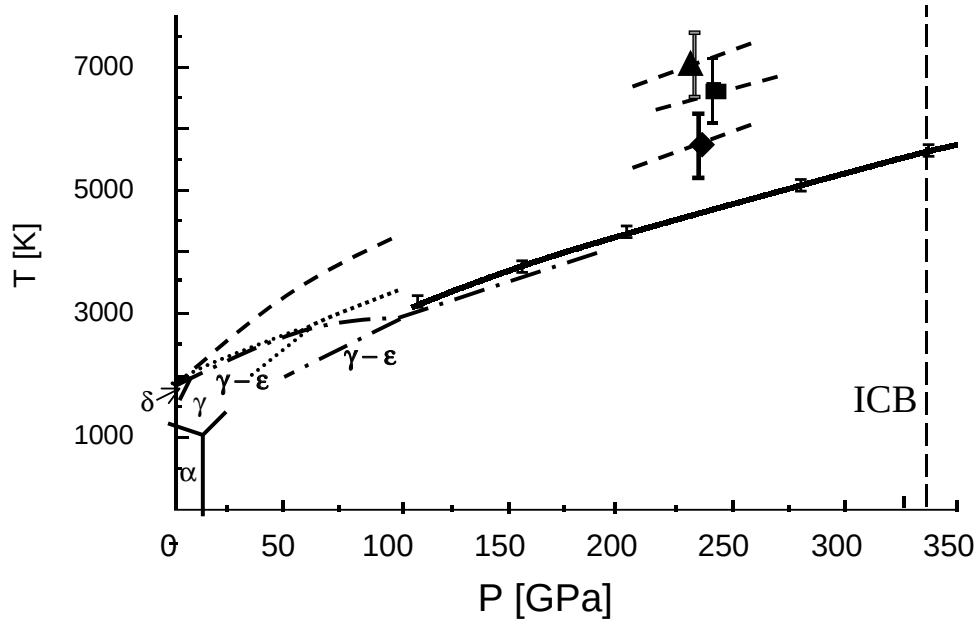

Figure 4.1: High-pressure melting line of iron. Theoretical melting line: thick full line with error bars. Other lines: DAC melting lines (same line code as in figure 1.1). Error bars with symbols: shock-waves melting points (same line code as in figure 1.1).

The calculated melting line of h.c.p. iron from 100 to 330 GPa is reported in Figure 4.1. Our melting temperature is in excellent agreement with laser-heated DAC experiments[31–33], available up to 200 GPa. At the ICB pressure (330 GPa) we find that h.c.p. iron melts at 5400 (± 100) K, only slightly higher than the value proposed by Boehler (4900K) extrapolating his DAC melting line up to 330

GPa[31]. On the other hand, our value for T_m at the ICB is in clear discrepancy with higher T_m values extracted from shock-wave data[34, 36]. We will see in Section 4.5 that shock-wave compression data, for what concerns densities, sound velocities and pressure, are actually in good agreement with our results, and that the disagreement concerns only the temperature. As we already pointed out in the Section 1.2.2, temperature in shock wave experiments is can be only measured by indirect methods[34, 36], possibly affected by systematic errors. This might explain the observed discrepancy, suggesting a reinterpretation of this class of results.

At 330 GPa the calculated density jump $\Delta\rho/\rho$ upon melting is 1.6 (± 0.1) %. Approximately the same value is observed at lower pressures. The error on $\Delta\rho$ due to the OP procedure is smaller than that on ρ because density jumps turn out to be much less dependent on the choice of the OP than absolute densities (see Table II of Chapter 3). Concerning the overall accuracy of our theoretical density jump, it should be noticed that, as we will see in Section 4.5, the density *difference* between solid and liquid phases 130 GPa and 3000 K far apart along the shock-wave compression line is overestimated by 0.3 % only with respect to experimental data. An even better predictivity is expected in a static melting process, where pressure and temperature are unchanged. Thus it is likely that the overall error in $\Delta\rho/\rho$ is not so different from the intrinsic OP error of 0.1 %.

The heat of melting (ΔH_m) at 330 GPa is 0.7 $(\pm 0.05) \times 10^6$ J/Kg, also rather independent of the OP. This coincides with ΔH_m as extracted, through the Clausius-Clapeyron equation, from the density jump and our slope of the melting line ($dT_m/dP \simeq 10$ K/GPa). The heat of melting is distinctly smaller than elsewhere suggested [4, 9], except for estimates based on dislocation theory[19].

Since ΔH_m is proportional to $\Delta\rho$ through Clausius-Clapeyron, the accuracy on this quantity is expected to be the same as the accuracy on $\Delta\rho$. With our value for ΔH_m, the iron-freezing contribution to the geodynamo should be smaller than suggested[9] or, alternatively, the inner-core lifetime should be shorter.

The entropy of melting ΔS_m is $0.86\ k_b$. This value is, once again, quite small compared with previous estimate [4]: melting of iron at high pressure conditions is a process with very small jumps of all the thermodynamic observables at phase transition (in Section 4.4 we shall see that also the shear modulus of the solid phase at melting is very small). For a close packed solid with small volume jump at melting, the value of the entropy of melting can also be estimated by the relation[10]

$$\Delta S_m = k_b \ln 2 + \alpha B_T \Delta V_m$$

where B_T is isothermal bulk modulus, α is the thermal expansion coefficient, ΔV_m is the volume jump at melting, and $k_b \ln 2$ is the entropy of disorder due to the existence of line defects in the liquid that are absent in the solid, and is the only term that survives for vanishing ΔV_m. With our values of α and B_T ($\sim$ 1.6 10^{-5} K^{-1} and 1400 GPa respectively at 330 GPa and 5400 K) , ΔS_m as estimated with this relation is 0.87 k_b, in excellent agreement with the direct calculation. This further confirms the overall consistency of our model of iron at ICB conditions. It is also remarkable that the contribution to ΔS_m of the volume jump is 0.18 k_b only, so that purely topological entropy dominates ($\ln 2\, k_b \sim 0.69\ k_b$).

4.3 Density of iron at ICB conditions

The density of solid iron at 330 GPa and 5400 K is found to be 13.0 (± 0.1) gr/cm^3, about 2 % larger than the density of the inner core at the ICB (12.76 gr/cm^3, ac-

cording to the PREM model[3]), supporting the presence of lighter elements in the inner core[17]. For liquid iron we find, at 330 GPa and 5400 K, a density of 12.80 (± 0.1) gr/cm^3. The difference between the calculated liquid iron density at 330 GPa and T$_m$ and the PREM value for the Earth's outer core density(12.166 gr/cm^3) is ~ 5 % (this difference crucially constraining the amount of lighter elements in the Earth's outer core). The values commonly assumed for this difference are rather higher (7 - 10 %) [9, 16]. Keeping into account a possible systematic underestimation of ~ 1 % in our density data, as it can be deduced from zero temperature EOS data (see Chapter 2) and Hugoniot data (see Section 4.5), our theoretical estimate for the density deficit in outer core is ~ 6 %. We find therefore that only the lowest values among those commonly assumed are compatible with our result. [2]

As we already discussed in Section 4.2, the presence of lighter elements will necessarily change the melting temperature of the composite alloy with respect to T_m of pure iron. If ideal mixing between iron and the impurity is assumed, the melting temperature T$_{all}$ of the alloy can be estimated by[4, 10]

$$\ln(1-x) = \frac{\Delta H_m}{k_b}\left(\frac{1}{T_m} - \frac{1}{T_{all}}\right) \tag{4.4}$$

where x is the concentration (molar percentage) of the impurity, k_b is the Boltzmann constant, ΔH_m is the heat of melting of pure iron and T$_m$ its melting tem-

[2]Concerning the reliability of our predictions for the density deficit in outer and inner core with respect to pure iron, it has to be noticed that the PREM itself may not be accurate to the 1 % level. PREM values for the densities are deduced within a model in which the value of some variables is not *calculated* but *assigned*[3, 10]. This is the case of the density jump at ICB (assumed to be of 0.5 g/cm^3) and of the value for the density at the base of the mantle (assumed to be 5.5 g/cm^3). Thus, comparison with the PREM, although fully meaningful, may not allow for very precise determinations of the core density deficit.

perature. The concentration x can be estimated by the relation

$$\frac{x\, m_{imp} + (1-x)\; m_{Fe}}{x\, \frac{m_{imp}}{\rho_{imp}} + (1-x)\; \frac{m_{Fe}}{\rho_{Fe}}} = \rho_{PREM} \tag{4.5}$$

where m_{imp} and m_{Fe} are the atomic weight of the impurity and of iron, ρ_{imp} and ρ_{Fe} are their densities at ICB conditions. We have used room-temperature equation of state data for FeO, Si and FeS[10] in order to estimate ρ_{imp}, and the molar fraction x of these impurities (by eq. (4.5)). The corresponding melting temperature T_{all} in ideal mixing conditions (deduced by eq. (4.4)) is reported in table:

	ρ_{Fe}/ρ_{imp}	x	T_{all} [K]
Fe0	1.3	.16	4500
FeS	1.37	.11	4750
Si	2.15	.099	4810

T_{all} would coincide with the Earth temperature at the inner core boundary if a single impurity would be present. However, it has to be noticed that while impurity density values as obtained from room temperature equations of state are probably very reasonable, ideal mixing is a strong hypothesis, often violated in real systems (e.g. in Fe-Si at zero pressure[10]). For this reason these temperatures have to be considered only rough estimates.

4.4 High temperature elastic properties

The calculation of sound velocities for hcp iron at inner core conditions is relevant for geophysics, since bulk and shear velocities of the Earth's core are the only quantities that can be directly measured by seismological methods[3]. The presence of impurities in the inner core ($\sim 2\%$, as we have seen) could, in principle,

slightly modify the elastic properties. Nevertheless, like for the melting temperature, the properties of pure iron are an important reference for any elastic model of the inner core.

High temperature elastic constants are calculated, following Parrinello and Rahman [82], by performing long classical runs ($\sim$500 ps) at constant pressure on solid samples of $\sim$1000 atoms with a potential optimized in the given P-T conditions. The sample is thermalized at the temperature of interest. In the 500 ps run, however, the temperature is not controlled. In these conditions, *adiabatic* elastic constants are obtained from strain fluctuations in a constant-pressure MD run:

$$C_{ij} = \frac{k_B T}{V} \langle \epsilon_i \epsilon_j \rangle^{-1}$$

where ϵ_i is related to the strain tensor ε_{ij} by the relations (4.2). The strain tensor is defined with respect to a reference cell that, by definition, is the cell averaged on the whole run. Thus, we have [82]

$$\varepsilon = \frac{1}{2} \left(\mathbf{h}_0^{t\,-1} \mathbf{h}^t \mathbf{h} \mathbf{h}_0^{-1} - 1 \right)$$

where $\mathbf{h}$ are the cell variables and $\mathbf{h}_0 = \langle \mathbf{h} \rangle$. Shear and bulk sound velocities (or, equivalently, shear and bulk moduli) are then computed using Voigt relations (4.2) and (4.3). As a test for the consistency of the method, we have also calculated the bulk modulus by the alternative expression [82]

$$B = \frac{k_B T V_0}{\left\langle (V - V_0)^2 \right\rangle}$$

where V is the volume of the cell and $V_0 = \langle V \rangle$. The value obtained by this relation and by eq. (4.2) compare within 1 %.

Calculated bulk and shear moduli for hcp iron at 330 GPa and 5400 K are compared with seismological measurements [3] in Figure 4.2. Our theoretical

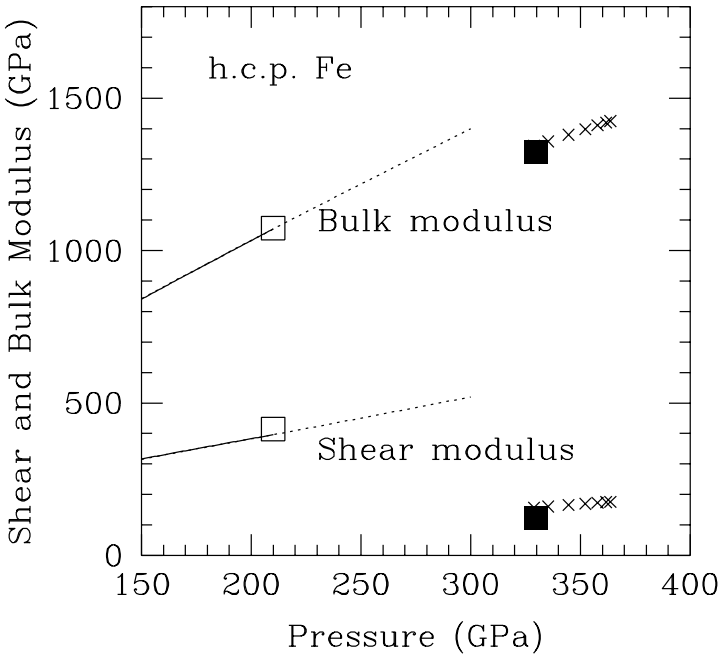

Figure 4.2: Voigt averages(4.2), (4.3) of shear and bulk moduli for compressed solid iron, as compared with inner-core data and DAC experiments. Lines: room temperature DAC data [5] (full line: actual data; dashed line: extrapolation). Open squares: this work (room temperature). Crosses: seismic observations for the inner core[3]. Full squares: this work (melting temperature). The error bars are given by the size of the squares.

values are very close to the seismological values. The 210 GPa room temperature data are also reported on the same figure for comparison. This finding is somehow unexpected for what concerns the shear modulus. In fact, it has been noted that the value of shear modulus in the solid inner core is anomalously low for a closed-packed phase, leading to suggestions that additional low-shear phases may be present there, other than h.c.p. [5, 25]. In a lot of solid metals, the shear modulus at melting shows, at zero pressure, a reduction of less than 50 % from its low temperature value [24]. The inner core shear modulus [3] displays a threefold reduction with respect to low temperature measurements[5] and calculations[23] in pure Fe. Our data show that the shear modulus of compressed h.c.p. iron close to melting is perfectly compatible with seismic data.

This decreased shear modulus fits very well a Born-Durand picture of melting[24]. According to this picture, the isobaric thermal dilatation within the solid phase and after melting is linearly correlated with the drop of shear modulus. This empirical law is apparently verified in a large class of systems, ranging from molecules, rare gases, insulators and metals[24]. As shown in Figure 4.3, also the shear modulus of iron follows closely this law, even if, in comparison with standard metals, compressed iron melts much closer to the mechanical instability (vanishing shear modulus), which clearly correlates with the small volume jump at melting.

4.5 Calculation of iron shock-wave compression line

The shock wave compression line (the so called Hugoniot) is a very reliable source of informations concerning the high temperature properties of materials. Density, pressure and sound velocities are either measured directly, or related to impactor

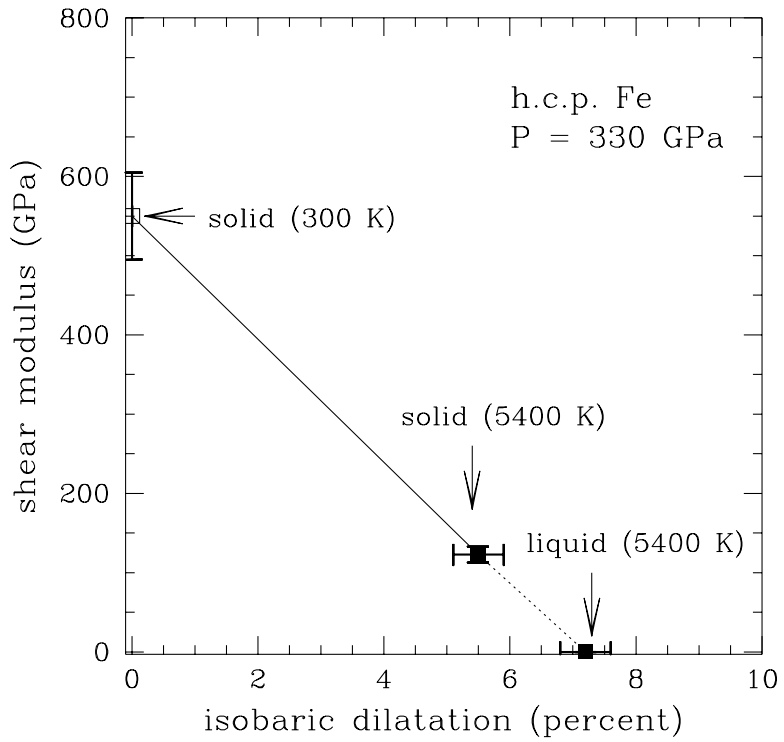

Figure 4.3: Behavior of the shear modulus of h.c.p. iron as a function of the isobaric thermal dilatation. Open square: X-ray diffraction measurements[5]. Filled squares: theoretical results. The lines are guides to the eye.

speed by simple thermodynamic relations. The measurement of sound velocity and densities along the Hugoniot for iron up to ~ 400 GPa by Brown and McQueen in 1985[13] is considered a cornerstone result for high pressure physics of iron. The observed double kink in wave velocity (at ~ 200 GPa and ~ 240 GPa) led them to suggest the presence of a new high-pressure high-temperature phase between the ε phase and melting. This has inspired a large amount of research in the last fifteen years. Indeed, up to now, their observation has never been con-

firmed unambiguously. On the other hand, theoretical works based on classical molecular dynamics [28] have suggested that the double kink in sound velocities could be a by-product of phase coexistence, therefore strongly dependent on experimental conditions.

Another observable of fundamental importance is the value of the temperature along the Hugoniot. A reliable estimate of this quantity, together with a correct interpretation of wave velocities discontinuities, would be equivalent to an experimental measurement of high pressure melting temperature of iron. Unfortunately, at variance with pressure and wave velocities, temperature in a shock-wave experiment can be measured only indirectly[36], with possibly large systematic errors, or estimated without keeping into account phase transition[13, 56].

In this Section we introduce a method for calculating a shock-wave compression equation of state of iron by a suitable use of the optimal potentials. In this way, we provide the first theoretical estimate of the temperature along the Hugoniot explicitly keeping into account phase transitions.

In a standard shock-wave experiment, the quantities that are measured are the shock-wave velocity (U_s) and the velocity imparted to the particles of the sample by the shock wave (U_p). By assuming conservation of energy, mass and momentum in the shocked sample, pressure P, internal energy U and density ρ during the shock can be deduced from these velocities by the so-called Rankine-Hugoniot equations[10]:

$$\begin{aligned} \rho &= \frac{\rho_0 U_s}{U_s - U_p} \\ P &= \rho_0 U_s U_p \\ U &= U_0 + \frac{1}{2} U_p^2 \end{aligned}$$

(U_0 and ρ_0 are internal energy and density of the sample before the shock). These

relations are very useful and reliable, since both U_P and U_S can be measured with great accuracy. U_s and U_p can be eliminated from these relations, taking to the so-called Hugoniot equation of state:

$$\frac{1}{2}P\left(V_0 - V\right) = U - U_0 \tag{4.6}$$

(V is the atomic volume). It should be noticed that thermal equilibrium has to be assumed in order to derive the Hugoniot-Rankine relations, but this hypothesis is very likely to be verified almost exactly in shocked samples, as it was shown, e.g., by the theoretical calculations of Belonoshko[28].

At high temperature, both V and U have to be computed as averages on long runs that cannot be afforded within a fully ab-initio description of iron. Therefore, we solved equation (4.6) by a suitable use of the optimal potential technique.

The volume V and internal energy U corresponding to a given pressure P were calculated by the following iterative procedure:

1. a first trial temperature $\widetilde{T}$ was assumed, and an OP at $\left(P, \widetilde{T}\right)$ was generated; the corresponding atomic volume $\widetilde{V}$ was directly calculated. The internal energy, at variance with $\widetilde{V}$, cannot be directly computed as an average over the OP run, since the zero of the energy for the classical potential is arbitrary. This arbitrariness is eliminated by refering all the energies to the unique quantum energy scale. Thus, the internal energy $\widetilde{U}$ corresponding to the trial temperature $\widetilde{T}$ is calculated by

$$\widetilde{U} = E_{ai}^{ref} - E_{OP}^{ref} + \frac{3}{2}k\widetilde{T} + \langle E_{OP} \rangle$$

where E_{OP}^{ref} is the OP energy in a reference configuration, E_{ai}^{ref} is the ab-initio energy in the same configuration, and $\langle E_{OP} \rangle$ is the OP energy av-

eraged on a run at pressure P and temperature $\widetilde{T}$ (see Section 3.4 for an estimate of the accuracy of this procedure).

2. If $\widetilde{U}$ and $\widetilde{V}$ don′t satisfy the Hugoniot equation, a new trial temperature was estimated by the relation

$$\frac{1}{2}\left[P\left(V_0-\widetilde{V}\right)+\widetilde{P}dV\right]=\widetilde{P}dV+C_P dT+\widetilde{U}-U_0$$

where dV and dT are the volume and temperature change from $\widetilde{V}$ and $\widetilde{T}$ that are required in order to satisfy (4.6). Since the volume change can be estimated by the relation $dV=\widetilde{V}\alpha dT,$ where α is the thermal expansion coefficient, the new trial temperature $\widetilde{T}_{new}$ was estimated by

$$dT=\widetilde{T}_{new}-\widetilde{T}=\frac{\frac{1}{2}\left[P\left(V_0-\widetilde{V}\right)\right]-\left(\widetilde{U}-U_0\right)}{\frac{1}{2}P\widetilde{V}\alpha+C_P}.$$

The procedure was iterated until the difference $\frac{1}{2}P\left(V_0-\widetilde{V}\right)-\left(\widetilde{U}-U_0\right)$, evaluated at the temperature $\widetilde{T}_{new}$ was below ~ 100 K, i.e. the usual accuracy that can be obtained by the OP procedure. Since C_p and α were known, at least approximately, from previous calculations, usually no more than two iteration were required in order to satisfy condition (4.6).

Relation (4.6) can be easily generalized to include the possibility of phase coexistence. In particular, if, at a pressure P and a temperature T_{tr}, the system can exist in two distinct phases A and B (e.g. liquid and hcp), the volume per atom and the internal energy have to be estimated in both phases. Denoting these quantities by $\widetilde{V}_A$, $\widetilde{V}_B,\widetilde{U}_A$ and $\widetilde{U}_B$ respectively, the molar percentage x_A of phase A along the shock-wave compression line is solution to the equation

$$\frac{1}{2}\left[P\left(V_0-x_A\widetilde{V}_A-\left(1-x_A\right)\widetilde{V}_B\right)\right]=x_A\widetilde{U}_A+\left(1-x_A\right)\widetilde{U}_B-U_0.$$

If this equation admits a solution smaller than one and positive, the volume per atom and internal energy satisfying the Hugoniot equation (4.6) are

$$\begin{aligned} \widetilde{V} &= x_A \widetilde{V}_A + (1 - x_A)\, \widetilde{V}_B \\ \widetilde{U} &= x_A \widetilde{U}_A + (1 - x_A)\, \widetilde{U}_B \end{aligned}$$

The Hugoniot equation of state calculated with this procedure is compared with experimental data in Figure 4.4 and 4.5. Shocked iron remains solid up to a pressure of 195($\pm$5) GPa. At this pressure, the temperature is 4000 K, and corresponds to the melting temperature of h.c.p. iron. Between 195($\pm$5) GPa and 280($\pm$5) GPa the system along the shock-wave compression line displays phase coexistence. In this range of pressure, the supplemental energy due to the increasing speed of the bullet melts more and more percentage of the system, while the temperature, by definition of equilibrium, remains identically equal to the melting temperature. The molar percentage of liquid iron was calculated at 200 GPa, 220 GPa, 240 GPa and 280 GPa and increases with pressure almost linearly in the range of pressure considered. Above 280 GPa the system is totally molten. It has to be remarked that experimental and theoretical stability range along the Hugoniot for ε phase and for liquid phase coincide within 5 GPa, as it is evident from Figure 4.4.

The density as a function of pressure on the calculated and experimental shock-wave compression line are compared in Figure 4.4 (top). The agreement is always better than 1.4 %, with slightly better agreement at lower pressures. The theoretical density is always underestimated with respect to the experimental one, so that density differences are reproduced within an agreement of 0.3 % for every pressure. This results strenghtens our predictions concerning density of iron at inner core boundary conditions: $\sim$1 % is a small error, of the order of magnitude

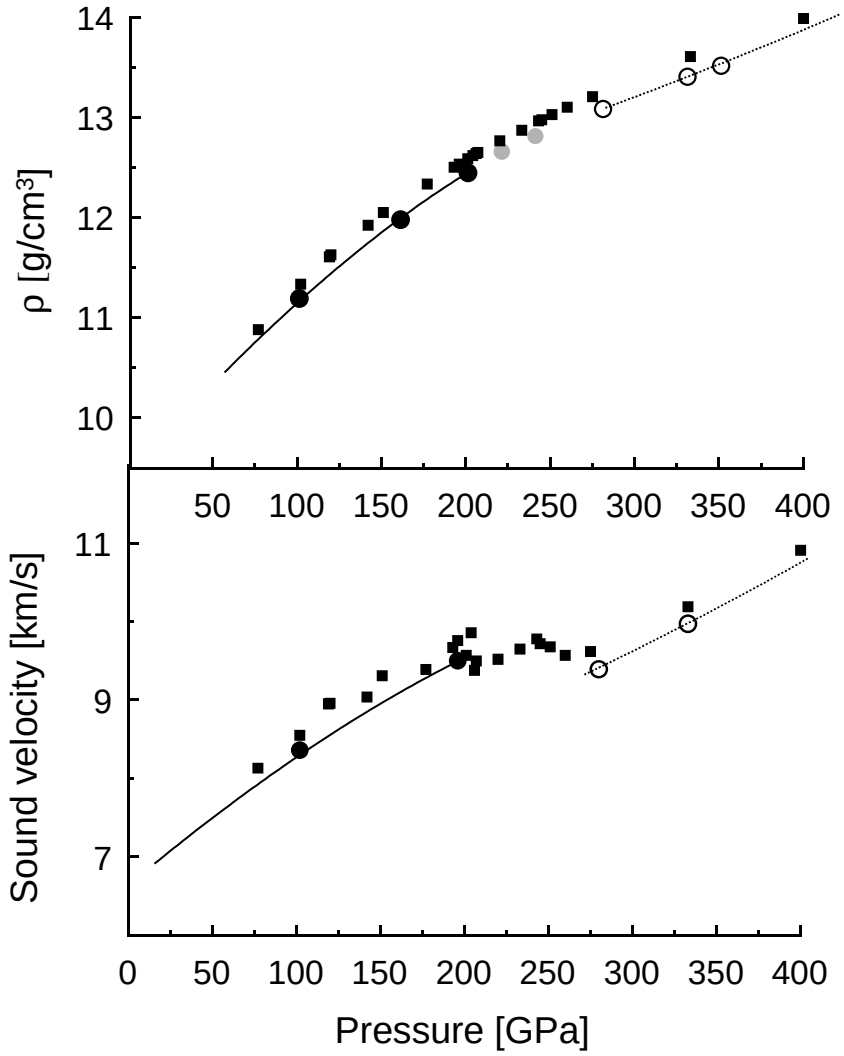

Figure 4.4: Densities (top) and sound velocities (bottom) along the Hugoniot. Full squares: experiments[13]; circles: theory. Full circles correspond to solid (hcp) iron; empty circles to liquid iron; gray circles correspond to systems in phase coexistence regime. The full line and the dotted line are guides to the eye.

of state-of-the-art ab-initio calculations. Moreover, the same underestimate is obtained also for room temperature densities (see Figure 2.1), and it is probably due to the GGA approximation or to insufficient k-points sampling in calculating the electronic wave-function

Experimental and theoretical sound velocities are compared in Figure 4.4 (bottom), showing that our method is able to reproduce the experimental values within 3 %, both in the solid and in the liquid phase. No attempt is done to estimate v_s in the phase coexistence region.

In Figure 4.5, the temperature along the shock-wave compression line, as calculated with our method is plotted together with the same quantity as measured by Yoo *et al* [36], Bass *et al* [34], and as computed by Brown and McQueen[13] on the base of simple thermodynamics and without keeping into account possible phase transitions. The agreement of our results with Yoo's data is not good, especially at low pressure. At 260 GPa (i.e. at the pressure that is claimed to be the Hugoniot melting pressure by Yoo *et al*), the calculated temperature is $\sim$ 4650 K, about 2000 K below the measured temperature at this pressure. This discrepancy suggests a need for reinterpretation of this class of experimental data, also in view of the excellent agreement of our calculations with DAC measurements for what concerns the melting temperature. Our data are instead in excellent agreement with Brown and McQueen's predictions up to 200 GPa (their estimate is in fact based on very reasonable assumptions on the values of the Gruneisen parameter and C_v). Above 200 GPa, Brown and McQueen's temperatures continue to grow almost linearly (they neglect any latent heat due to phase transformations), while a substantial change of slope, due to phase coexistence between 195 and 280 GPa, is observed in our data at 195 GPa. In particular, the temperature coincides in this

range of pressure with the melting temperature, by definition of thermal equilibrium. Above 280 GPa, the system is no more pinned to the melting temperature, and T grows with a slope higher than the slope observed in solid iron.

All of this provides, in our opinion, a satisfactorily framework to interpret the available experimental data on iron Hugoniot: our method is able to reproduce all the experimental data (densities, sound velocities, stability field of the ε phase and of the liquid phase along the Hugoniot) , with the exception of temperature measurements by Yoo *et al*[36] and by Bass *et al* [34]*if the region along the Hugoniot between the last observed point in the ε phase (~ 200 GPa) and the first observed point in the liquid phase (~ 280 GPa) is interpreted as a phase-coexistence region,* where the temperature is pinned to the melting temperature and sound velocities are not univocally defined, since the sample is non-uniform.

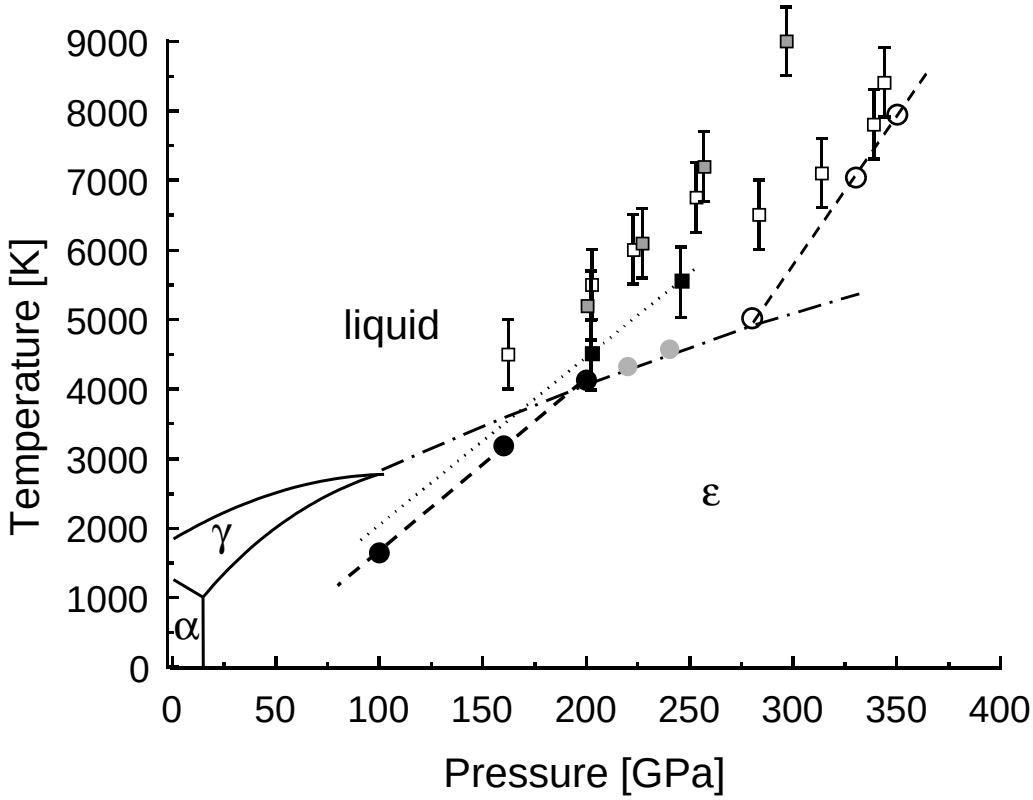

Figure 4.5: Temperature along the Hugoniot. Gray squares: experimental values from Bass *et al* [34]. Empty squares: experimental values from Yoo *et al* [36]. Full squares and black dotted line: estimate by Brown and McQueen based on simple thermodynamics (the two squares correspond to the discontinuities in the sound velocity)[13]. Circles: theory. Black corresponds to solid (hcp) iron; empty circles correspond to liquid iron; gray to systems in phase coexistence regime. The dashed lines are guides to the eye. The dash-dotted line corresponds to our theoretical melting line.

Summary and Conclusions

Since the core of the Earth is mainly composed of iron diluted with lighter elements, and since a solid-liquid interface exists inside the core (the inner core boundary) properties of iron close to melting at core pressures are directly related to properties of Earth's core. In this thesis we have discussed in details some of these properties that are of particular relevance for geophysics. In particular, we have considered the melting line, the density of liquid and solid iron, the elastic properties of solid iron at inner core pressures and the heat of crystallization at ICB pressure. All of these quantities were known from experiments and previous theoretical calculations only very approximately, as we have seen in Chapter 1, and therefore a careful theoretical evaluation will probably prove very helpful in improving the accuracy of Earth's core models.

The method employed here to provide an estimate of these quantities is based on the combined use of first-principle and classical molecular dynamics simulations.

A correct account of the electronic structure at the ab-initio level is fundamental for an accurate and reliable description of the dynamical properties of iron at Earth's core conditions[23, 43, 49]. Our calculations, as we discussed in Chapter 2, are based on a finite-temperature extension of density-functional theory within the gradient-corrected local density approximation, and on a pseudopotential de-

scription of the valence electron interaction with the ion core (nucleus plus $1s$, $2s$, $2p$ atomic core states). This theoretical approach gives a low temperature pressure-vs-density curve for hcp iron in excellent agreement with X-ray data[12] (first-principle densities are ~ 1 % smaller than experiment at all pressures). However, finite temperature properties can hardly be extracted from brute force first-principles simulations, due to the short simulation times (a few picoseconds) that can be afforded nowadays[49].

In this work we make use of the large amount of informations provided by first-principles simulations to construct a classical potential for iron with an explicit dependence on the thermodynamic P-T conditions. The potential, which includes genuine non-two-body terms [77, 78] and angular forces [77], is accurately optimized to reproduce the dynamics of iron *at that* P-T condition, by imposing the matching between classical and first-principles forces and stress in the framework of a suitable self-consistent (iterative) procedure described in Chapter 3. The full dynamical and thermodynamical properties of iron at a given P-T condition are then easily extracted from extensive classical molecular dynamics simulations. The "optimal potential" (OP) constructed in this way will not be transferable to different P-T conditions, where a different potential must be constructed. Our approach is thus totally different from previous attempts to estimate the melting temperature of iron based on classical potentials[25, 78], where a single potential is used at all P-T conditions.

Some examples of the ability of an OP to reproduce ab-initio quantities are provided in Chapter 3. E.g. , first-principle energy differences and stress are reproduced by the OP with an accuracy always better than 100 K and 1 GPa respectively (Figure 3.4 and 3.5).

The calculated melting line of hcp (ε-phase [33]) iron from 100 to 330 GPa is reported in Figure 4.2. Our melting temperature is in excellent agreement with laser-heated DAC experiments[31–33], available up to 200 GPa. At the ICB pressure (330 GPa) we find that hcp iron melts at 5400 (± 100) K, only slightly higher than Boehler's extrapolation (4900 K)[31]. On the other hand, our value for T_m at the ICB is in clear discrepancy with higher T_m values extracted from shock-wave data[30, 36], suggesting a need for reinterpretation of this class of experiments, also because, as discussed below, our theoretical data for density, pressure and sound velocities along the shock-wave compression line are instead in very good agreement with experiments.

The heat of melting (ΔH_m) at 330 GPa is 0.7 $(\pm 0.05) \times 10^6$ J/Kg respectively. ΔH_m is distinctly smaller than elsewhere suggested [4, 9], except for estimates based on dislocation theory[19]. With our value for ΔH_m, the iron-freezing contribution to the geodynamo should be smaller than suggested[9] or, alternatively, the inner-core lifetime should be shorter.

For the solid, we calculated the bulk and the shear moduli of hcp iron at T_m, and found them (Figure 4.2) to be in good agreement seismic data for the inner core, thus invalidating suggestions of a partially molten or glassy inner core.

The density of solid iron at 330 GPa and 5400 K is found to be 13.0 (± 0.1) gr/cm^3, about 2 % larger than the density of the inner core at the ICB (12.76 gr/cm^3, according to the PREM model[3]), supporting the presence of lighter elements in the inner core[17] Moreover, we find for liquid iron at 330 GPa and 5400 K a density of 12.80 (± 0.1) gr/cm^3. The difference between the calculated liquid iron density at 330 GPa and T$_m$ and the PREM value for the Earth's outer core density(12.166 gr/cm^3) is ~ 5 %. This difference crucially constrains the amount

of lighter elements in the Earth's outer core. By considering our systematic underestimation of ~ 1 % in the density, we find that only the lowest value among those commonly assumed (i.e. 7 - 10 % [9, 16]) is compatible with our result.

Finally, we provide the first-principles-quality determination of the Hugoniot EOS for iron which explicitly takes into account melting and is not restricted to the solid portion, as in previous works[56]. The calculated density along the Hugoniot are ~ 1 % smaller than the experimental one[13] both in solid and liquid phases (Figure 4.4). The theoretical sound velocities are also ~ 3 % smaller than the experimental ones. These errors are small for a first-principle calculation. Moreover, the error on the density is systematic and thus does not affect density differences. Our calculations suggest a reinterpretation of Brown and McQueen's data for sound velocities along the Hugoniot[13]. We find that the first kink (at 195 GPa) in Brown and McQueen's data is related to melting rather than to a solid-solid transition. The Hugoniot would then intercept the melting line at 195 GPa and 4100 K, in nice agreement with the DAC melting results[31], thus reconciling Brown and McQueen's shock-wave measurements with static DAC data. We suggest that the second kink observed by Brown amd McQueen is not associated with a phase transition, but may rather be a by-product of the phase coexistence between the solid and the liquid, as suggested by MD simulations performed on Argon by Belonoshko[28] and thus strongly dependent on experimental conditions. This scenario would be confirmed by the recent repetition of Brown amd McQueen experiment, by Nguyen and Holmes where the second kink is no more observed[29].

In conclusions, our results provide a satisfactorily framework to interpret most of the available experimental data on high P-T iron: our method is able to repro-

duce all these data (densities, sound velocities, stability field of ε phase and liquid phase along the Hugoniot, DAC melting temperatures where available), with the exception of temperature measurements in shock-wave experiments[34, 36].

The optimal potential method, applied in this work to study the high-pressure high-temperature physics of iron, could be of some help also for other applications, whenever the system size is to big for a fully ab-initio molecular dynamic simulation, but a very good accuracy in the determination of thermodynamical quantities is required.

Appendix A

Self-consistency methods for minimizing the free-energy functional .

At least two strategies are commonly used to calculate the ground state of 2.7. In the so-called *direct methods*, the minimum of the free energy functional is found directly, e.g. by a suitable preconditioned second order dynamics for the wave functions' degrees of freedom[71] or by a DIIS minimization[72]. In contrast with these methods, in the so-called self-consistency methods[68] the problem of minimizing the free energy functional is split into two problems: an iterative diagonalization of the Hamiltonian at fixed potential and an iterative improvement of the potential, based on a suitable mixing scheme for the charge density.

In this Appendix we will describe the self-consistent minimization method introduced by Kresse *et al*[68] and used in this work. At the beginning of the calculation, a reasonable set of trial wave functions and charge density is chosen.

In the absence of a better guess, the atomic wave functions and the relative charge density are used. Then, leaving the charge density (i.e. the potential) fixed, the KS problem $H_{KS}\left|\Psi_i\right\rangle = \varepsilon_i \left|\Psi_i\right\rangle$ is solved (in the so-called "internal cycle"). When this problem is solved within a fixed accuracy, a new electronic density $\rho_{out}\left(\{\Psi_i\}\right)$ =$\sum_i f_i \left|\Psi_i\left(r\right)\right|$ is computed.

The new electronic density and the new potential H_{KS} are constructed as a function of ρ_{out} and of the densities at the previous steps by a suitable mixing procedure (the so-called "external cycle"), and the procedure is iterated to self-consistence.

A.1 The internal cycle: DIIS diagonalization of Kohn-Sham Hamiltonian.

The goal of the internal cycle is to diagonalize the Kohn-Sham Hamiltonian H_{KS}, with fixed potential. In a case of a plane-wave basis set $\left\{\left|\mathbf{G}\right\rangle = e^{i\mathbf{G}\cdot\mathbf{r}}\right\}$, direct diagonalization is unfeacible because of the extremely large size the N×N Hamiltonian matrix (N> 10^3). However, diagonalizing H_{KS} is equivalent to minimize with respect to the wave functions the quantity $\sum_{i=1}^{N_b}\left\langle\Psi_{\,i}\right| H_{KS}\left|\Psi_{\,i}\right\rangle$, and then perform a unitary transformation on the wave functions in order to take the matrix $\left\langle\Psi_{\,j}\right| H_{KS}\left|\Psi_{\,i}\right\rangle$ to a diagonal form (the KS energies ε_i will be the eigenvalue of this matrix). Several approaches have been developed in order to speed up the above minimization. We outline here the DIIS procedure.

In the standard steepest-descent dynamics, at step $n+1$, the new wave function $\left|\Psi_i^{n+1}\right\rangle$ would be given by

$$\left|\Psi_i^{n+1}\right\rangle = \left|\Psi_i^n\right\rangle - K\left|D_i^n\right\rangle \tag{A.1}$$

where $|D_i^n\rangle$ is the gradient in wave function space, defined by

$$|D_i^n\rangle = H_{KS}\,|\Psi_i^n\rangle \tag{A.2}$$

and K is a suitable preconditioning function, i.e. an operator of the form

$$K = \sum_{\mathbf{G}} k\,(G)\,|\mathbf{G}\rangle\,\langle\mathbf{G}|\,.$$

The best possible choice for the preconditioning function K would be, of course, the inverse of H_{KS}. This would yield to the solution of the problem in a single step, but, of course, at the cost of inverting H_{KS}. Thus, the preconditioning function K is chosen[72] as the inverse of the diagonal part of the Hamiltonian, or, more exactly, as

$$k\,(G) = \begin{cases} 1/H_{ks\,G,G} & \text{if} \quad G \geq G_c \\ 1/H_{ks\,G_c,G_c} & \text{if} \quad G < G_c \end{cases}$$

where G_c is a free parameter that can be adjusted to accelerate convergence. In the application to iron, we have checked that $G_c^2/2 = 1.5$ Hartree provides the best performance.

In the DIIS scheme[72], equation (A.1) is improved with the following procedure. An "optimal" residual vector $|D_i^{n,\,op}\rangle$ and wave function $|\Psi_i^{n,\,op}\rangle$ are determined in order to improve the efficiency of the search in wave function space, and the new wave function is defined as a function of $|D_i^{n,\,op}\rangle$ and $|\Psi_i^{n,\,op}\rangle$ by a steepest-descent like step of the form (A.1):

$$\left|\Psi_i^{n+1}\right\rangle = |\Psi_i^{n,\,op}\rangle - K\;|D_i^{n,\,op}\rangle\,. \tag{A.3}$$

where optimal wave functions and residual vectors are expressed as linear combinations of the residual vectors and wave functions of the m previous steps respectively, as

$$|\Psi_i^{n,\,op}\rangle \;\; = \;\; \sum_{l=n-m}^{n-1} \alpha_i^l \left|\Psi^l{}_i\right\rangle \tag{A.4}$$

$$\left|D_i^{n,\,op}\right\rangle \;=\; \sum_{l=n-m}^{n-1} \alpha_i^l \left|D^l{}_i\right\rangle$$

where the constraint $\sum_l \alpha_{li} = 1$ has been imposed and the coefficients α_i^l are chosen in order to minimize the norm of $D_i^{n,\,op}$. Conditions (A.4) are satisfied if the α_i^l-s are, for every i, the solution to the linear system

$$\begin{pmatrix} d_i^{n-m,\,n-m} & \cdots & d_i^{n-m,\,n-1} & 1 \\ \cdots & \cdots & \cdots & \cdots \\ d_i^{n-1,\,n-m} & \cdots & d_i^{n-1,\,n-1} & 1 \\ 1 & \cdots & 1 & 0 \end{pmatrix} \begin{pmatrix} \alpha_i^{n-m} \\ \cdots \\ \alpha_i^{n-1} \\ -\lambda \end{pmatrix} = \begin{pmatrix} 0 \\ \cdots \\ 0 \\ 1 \end{pmatrix}$$

where $d_i^{k,\,l} = \left\langle D_i^k \,\middle|\, D_i^l \right\rangle$.

This condition fully defines the new trial wave function $\left|\Psi_i^{n+1}\right\rangle$ as a function of residual vectors and wave functions at the previous steps. In fact, using (A.3) and (A.4), we have

$$\left|\Psi_i^{n+1}\right\rangle = \sum_{l=n-m}^{n-1} \alpha_i^l \left(\left|\Psi^l{}_i\right\rangle - K \,\left|D^l{}_i\right\rangle\right).$$

After a certain number of DIIS step (smaller than five in our implementation) the procedure is stopped, and the final set of wavefunctions $\left\{\left|\Psi_i\right\rangle, i = 1, \ldots, N_b\right\}$ is orthonormalized.

Finally, a rotation in wave functions space is performed in order to take the KS matrix $\left\langle \Psi_{\,j}\right| H_{KS} \left|\Psi_{\,i}\right\rangle$ to a diagonal form and the new occupation numbers f_i are calculated by (2.8).

A.2 The external cycle: charge mixing.

In the Kresse algorithm, the charge density used to upgrade the KS potential is defined as a function of the charge densities at previous steps by a DIIS-like dy-

namics performed also for the density. The role of the gradient (A.2) in the DIIS algorithm is played in the charge mixing scheme by the residue

$$R\left(\rho_{in}\right) = \rho_{out}\left(\rho_{in}\right) - \rho_{in} \tag{A.5}$$

where ρ_{in} is the density used to construct the potential and $\rho_{out}\left(\rho_{in}\right)$ is the density corresponding to the wavefunctions diagonalizing the potential (as obtained by the internal cycle). At convergence $R\left(\rho_{in}\right) = 0$, i.e. the charge density does not change on iteration.

Like in the DIIS scheme, the input charge ρ_n at step n is finally determined by a charge density mixing scheme applied on an optimal charge density ρ_n^{op} and an optimal residue $R\left(\rho_n^{op}\right)$

$$\rho_n = \rho_n^{op} + f\ R\left(\rho_n^{op}\right) \tag{A.6}$$

where f is a suitable preconditioning function of the form (in reciprocal space)

$$f\ \left(G\right) = A\frac{G^2}{G^2 + G_0^2}$$

where G_0 and A are suitable parameters. The weighting function is introduced in order to avoid charge sloshing due to the divergence for small G-s of the dielectric matrix in metals (with $A = 1$ and $G_0^2 = 4\pi\,\chi\,e^2$, where χ is the dielectric susceptibility, $f\left(G\right)$ would be the inverse of the dielectric constant for a free-electron gas)[68].

At step n the new optimal charge density is searched as a linear combination of all the previous densities ρ_l as

$$\rho_n^{op} = \sum_{l \leq n} \alpha_l \rho_l$$

with $\sum_{l \leq n} \alpha_l = 1$.

The coefficients α_l are determined in order to minimize the norm

$$\langle R\left(\rho_n^{op}\right)|R\left(\rho_n^{op}\right)\rangle = \sum_{l\leq n,\ k\leq n} \alpha_l\alpha_k \langle R\left(\rho_l\right)|R\left(\rho_k\right)\rangle$$

with the constraint $\sum_{l\leq n}\alpha_l = 1$ (linearity of the residual vector with respect to the charge density ρ_n is assumed). The optimal α_l are then given by

$$\alpha_i = \frac{\sum_{l\leq n} A_{li}^{-1}}{\sum_{l\leq n,\ k\leq n} A_{lk}^{-1}} \tag{A.7}$$

with $A_{lk} = \langle R\left(\rho_l\right)|R\left(\rho_k\right)\rangle$.

It has been proved that the convergence speed is greatly improved if the scalar products defining A_{lk} are calculated by a suitable metric weighting in different manner the different reciprocal space components. Thus, the scalar products between the residues (A.5) are computed in reciprocal space using a weighting factor of the form $\frac{G^2+G_1^2}{G^2}$, where G_1 is a parameter.

Thus, in a charge-mixing scheme, the input charge ρ_n at step n in reciprocal space has the form:

$$\rho_n = \rho_n^{op} + f\left(G\right)\ R\left(\rho_n^{op}\right) = \sum_{l\leq n}\alpha_l\left(\rho_l + f\ \left(G\right)R\left(\rho_l\right)\right) \tag{A.8}$$

where the α_l are defined by (A.7).

The implementation of (A.8) requires the storage in G space of charges and residues at all the steps of the minimization procedure. For practical purposes, the summation in (A.8) are limited to the 3-4 steps preceding step n. At step 1, the charge density ρ_1^{op} in (A.8) is either extrapolated linearly from charge densities at previous steps (in a molecular dynamics run) or constructed as a superposition of atomic charge densities.

Bibliography

[1] E.D. Williamson, L.H. Adams, J. Washington Acad. Sci., **13**, 413-428, (1923).

[2] F. Birch, J. Geophys. Res., **57**, 227-286, (1961).

[3] A.M. Dziewonski, Phys. Earth Planet. Inter. **25**, 297-356 (1981).

[4] O.L. Anderson and A. Duba, J. Geophys. Res., **102**, 22659-22669 (1997).

[5] H.-K. Mao, J. Shu, G. Shen, R.J. Hemley, B. Li, A.K. Singh, Nature **396**, 741-743 (1998); **399**, 280 (1999) (Erratum).

[6] R. Car and M. Parrinello, Phys. Rev. Lett., **55**, 2471 (1985).

[7] M.P. Allen, D.J. Tieldslay, *Computer Simulations of Liquids*, Clarendon, Oxford (1987).

[8] L. Vocadlo, G.A. de Wijs, G. Kresse, M.J. Gillan, G.D. Price, Faraday Discuss. **106**, 1 (1997).

[9] F. Stacey, *Physics of the Earth*, Brookfields Press, Australia (1992).

[10] J.-P. Poirier, *Introduction to the Physics of the Earth's Interior*, Cambridge University Press (1991).

[11] J.-P. Poirier, Phys. Earth Planet. Inter., **85**, 310-337, (1994).

[12] Mao, H.K., Y. Wu, L.C. Chen, J.F. Shu, and A.P. Jephcoat, J. Geophys. Res., **95**, 21737-21742, (1990).

[13] J.M. Brown and R.G. McQueen, J. Geophys. Res. **91**, 7485-7494 (1986).

[14] W.A. Bassett, Science, **266**, 1662-1663 (1994).

[15] D.E. Loper, Geophys. J.R. astr. Soc., **54**, 389-404 (1978).

[16] R. Jeanloz, Ann. Rev. Earth Planet. Sci., **18**, 357 (1990).

[17] A. Jephcoat and P. Olson, Nature, **325**, 332 (1987).

[18] S. Labrosse, J.-P. Poirier, J.-L. Le Mouel, Phys. Earth Planet. Inter., **99**, 1-17 (1997).

[19] J.-P. Poirier and T.J. Shankland, Geophys. J. Int., **115**, 147-151 (1993).

[20] J. Tromp, Nature **366**, 678-681 (1993).

[21] A.M. Dziewonski and F. Gilbert, Nature **234**, 465-466 (1971).

[22] S.-I. Karato, Science, **262**, 1708 (1993).

[23] L. Stixrude and R. Cohen, Science **267**, 1972-1975 (1995).

[24] J.L. Tallon, Phil. Mag. A, **39** , 151-161 (1979).

[25] M. Matsui and O.L. Anderson, Phys. Earth Planet. Inter., **103**, 55-62 (1997).

[26] Jephcoat, A., H.K. Mao, P.M. Bell, J. Geophys. Res., **91**, 4677-4684 (1986).

[27] S.C. Singh, J.-P. Montagner, Nature, **400**, 629 (1999).

[28] A.B. Belonoshko, Science **275**, 955 (1997).

[29] J.H. Nguyen, N.C. Holmes, A GU Abstract **79**, T21D-06 (1988).

[30] Q.R. Williams, R. Jeanloz, J. Bass, B. Swendsen, and T. Ahrens, Science **236**, 181-182 (1987).

[31] R. Boehler, Nature **363**, 534 (1993).

[32] S.K. Saxena, G. Shen, and P. Lazor, Science **264**, 405-407 (1994).

[33] A. Shen, H.-k. Mao, R.J. Hemley, T.S. Duffy, M.L. Rivers, Geophys. Res. Lett. **25**, 373-376 (1998).

[34] Bass, J.D., T.J. Ahrens, J.R. Abelson, T.Hua, J. Geophys. Res., **95**, 21757-21777 (1990).

[35] Ahrens, T.J., H. Tan, J.D. Bass, High Press. Res., **2** , 145-156, (1990).

[36] C.S. Yoo, N.C. Holmes, M. Ross, D. Webb, C. Pike, Phys. Rev. Lett., **70**, 3931 (1993).

[37] K.G. Gallagher, T.J. Ahrens, Abs. T 41F-9, Eos, **15** , Suppl. 653 (1994).

[38] R. Boehler, N. von Bargen, A. Chopelas, J. Geophys. Res., **95**, 21731-21736, (1990).

[39] R. Boehler, High-Pressure Science and Technology, edited by S.C. Schmidt, J.W. Shaner, G.A. Samara, and M. Ross, American Institute of Physics, Woodbury, New York, 919-922, (1994).

[40] Yoo, C.S., J. Akella, C. Ruddle, H.K. Mao, C. Meade, R. Hemley, Bull., Am. Phys. Soc., **39**, 147, (1994).

[41] O.L. Anderson, Rev. Geophys. Suppl., 429-441 (1995).

[42] M. Ross, D.A. Young, R. Grover, J. Geophys. Res., **95**, 21713-21716(1990).

[43] P. Söderlind, J.A. Moriatry, J.M. Willis, Phys. Rev. B, **53**, 14063-14072 (1996).

[44] L. Vocadlo, J. Brodholt, D. Alfe, G.D. Price, Geophys. Res. Lett., **26**, 1231-1234 (1999).

[45] Saxena, S.K., G. Shen, P. Lazor, Science, **260**, 1313 (1993).

[46] S.K. Saxena, L.S. Dubrovinsky, P. Haggkvist, Y. Cerenius, G. Shen, H.-k. Mao, Science, **269**, 1703 (1995).

[47] C.S. Yoo, P. Soderlind, J.A. Moriatry, A.J. Cambell, Phys. Lett. A, **214**, 65-70 (1996).

[48] D. Andrault, G. Fiquet, M. Kunz, F. Viscocekas, D. Hausermann, Science, **278**, 831 (1997).

[49] G.A. de Wijs, G. Kresse, L. Vocadlo, D. Dobson, D. Alfé , M.J. Gillan, G.D. Price, Nature, **392**, 805-807 (1998).

[50] H.J.F. Jansen, K.B. Hathaway, A.J. Freeman, Phys. Rev. B **30**, 6177 (1994).

[51] H.J.F. Jansen, K.B. Hathaway, A.J. Freeman, Phys. Rev. B **31**, 7603 (1995).

[52] A.D. Becke, Phys. Rev., **A 38**, 3098 (1988).

[53] J.P. Perdew, Phys. Rev., **B 33**, 8822 (1986).

[54] L. Stixrude, R.E. Cohen, D.J. Singh, Phys. Rev. B, **50**, 6442 (1994).

[55] E. Moroni and T. Jarlborg, Europhys. Lett., **33**, 223 (1996).

[56] E. Wasserman, L. Stixrude, R.E. Cohen, Phys. Rev. B, **53**, 8296 (1996).

[57] J.O. Hirshfelder, C.F. Curtiss, R.B. Bird,*Molecular theory of Gases and Liquids*, John Wiley aand Sons, Inc., New York (1954).

[58] D. Vanderbilt, Phys. Rev. B, **41**, 7892-7895 (1990).

[59] W.W. Anderson, T.J. Ahrens, J. Geophys. Res., **99**, 4273-4284 (1994).

[60] J.P. Poirier, Geophys. J., **92**, 99-105 (1998).

[61] R.T. Merrill, P.L. McFadden, J. Geophys. Res., **100**, 317-326 (1996).

[62] P. Hohenberg, W. Kohn, Phys. Rev., **136**, B864 (1964).

[63] W. Kohn, L.J. Sham, Phys. Rev., **140**, A1133 (1965).

[64] A. Fetter, J.D. Walecka, *Quantum Theory of Many-Particle Systems*, McGraw-Hill, New York (1971).

[65] M.L. Cohen, V. Heine, J.C. Phillips, *The Quantum Mechanics of Materials*, Scientific American, **246**, 66 (1982).

[66] N. Troullier, J.L. Martins, Phys. Rev. B, **43**, 1993 (1991).

[67] J.F. Annett, Comput. Mat. Sci., **4**, 23 (1995).

[68] G. Kresse, J. Furthmuller, Phys. Rev. B, **54**, 11169 (1996).

[69] N. Mermin, Phys. Rev., **137**, A1441 (1965).

[70] C.Cavazzoni, S. Cozzini, CINECA Report, 462-470 (1997).

[71] F. Tassone, F. Mauri, R. Car, Phys. Rev. B, **50**, 10561 (1994).

[72] J. Hutter, H.P. Luthi, M. Parrinello, Comp. Mat. Sci., **2** , 244 (1994).

[73] S.G. Louie, S. Froyen, M.L. Cohen, Phys. Rev. B, **26**, 1738 (1982).

[74] O. Sugino, R. Car, Phys. Rev. Lett., **74**, 1823 (1995).

[75] F. Ercolessi, J. B. Adams, Europhys. Lett., **26**, 583 (1994).

[76] M.S. Daw, M.I. Baskes, Phys. Rev. B, **29**, 6443 (1984).

[77] M.I. Baskes, Phys. Rev. B **46**, 2727-2742 (1992).

[78] A.B. Belonoshko and R. Ahuja, Phys. Earth Plan. Int. **102** , 171-184 (1997).

[79] O. Tomagnini, F. Ercolessi, S. Iarlori, F. D. Di Tolla, E. Tosatti, Phys. Rev. Lett., **76**, 1118 (1996).

[80] M. Parrinello and A. Rahman, Phys. Rev. Lett., **45**, 1196 (1980).

[81] N.W. Ashcroft, N.D. Mermin, *Solid State Physics*, Saunders College, Philadelphia (1976).

[82] M. Parrinello and A. Rahman, J. Chem. Phys. **76**, 2662 (1982).